# Aerodynamic Interaction of a Front and Rear Wheelhouse for a Generic Vehicle

by

**Radoje Radovic**

A thesis submitted to Macquarie University

for the degree of Master of Research

School of Engineering

November 2020

**MACQUARIE**
University
SYDNEY·AUSTRALIA

# Statement of Originality

I, Radoje Radovic, declare that the work presented has not been previously submitted for any academic assessment any university. To the best of my knowledge, the work in this thesis contains no material published by any other person except where references have been made.

Radoje Radovic

November 10th, 2020

# Acknowledgements

I would like to thank the following people for their support and assistance throughout the writing of this thesis.

I must thank my supervisor Dr Sammy Diasinos for your guidance and support throughout this project. Your feedback has been invaluable and our discussion about all things aerodynamics have pushed me to produce work you will be proud of. Thank you and I look forward writing with you again in the future.

Thank you to Macquarie University for offering me this Post-Graduate research position and providing a COVID relief grant. It has allowed me to produce work that can then live up to the high standards of the University.

I must thank my lovely partner Erika for her love and support throughout this thesis. You have given me perspective and driven me to achieve my very best and I look forward to our future together wherever the world may take us.

Mum, you have supported me through everything I have done and it means the world. You understood how important following my dreams always was and pushed me to do exactly that. Thank you.

I can't forget to thank my niece Alegra, your paper cranes have been perched on top of my monitors since I began the project and have watched over me from day one. Follow your dreams and you can achieve anything.

I'm looking forward to doing it all again. I know you all will be there for me and will do the same for you when the time comes.

# Abstract

Wheels produce key flow structures that contribute up to 30% of a vehicle's drag, limiting range and increasing emissions. The jetting vortices produced by the front wheels have been demonstrated to contribute greatly to the drag of a vehicle. Studies concerning wheels within a wheelhouse have often neglected the impact of the rear wheel and how the flow structures from the front wheel influence those generated at the rear. A numerical investigation was undertaken that utilised a modified Fabijanic body that included rear wheels. Variations in wheel spacing, front and rear overhang were evaluated that demonstrated these were critical geometric parameters that could vary the total vehicle lift and drag in excess of 100% and 15% respectively. Rear wheelhouse vortices displayed distinctive changes to those produced at the front wheel and were sensitive to wheel spacing. These changes were driven by the outboard jetting and inner wheelhouse outflow vortices which would suppress vortex formations at the rear wheel, manipulating the flow field and resulting in a significant change in overall drag force. Variations in wheel spacing and front overhang have demonstrated the significant impact of the front wheel flow structures on the rear wheel flow field and can be manipulated to reduce vehicle drag.

# Contents

# List of Figures

# List of Tables

# Nomenclature

$\alpha$          Transparency

$C_D$          Coefficient of Drag

$C_L$          Coefficient of Lift

$C_P$          Pressure Coefficient

$C_{PT}$          Total Pressure Coefficient

$f_1$          Fine grid solution

$f_2$          Coarse grid solution

$F_s$          Factor of Safety

$f_{exact}$          Exact solution

$I_{uu}$          Turbulence intensity

$k - \epsilon$          k-epsilon turbulence model

$k - \omega\ SST$          k-omega Shear-Stress Transport turbulence model

$l$          Turbulent length scale

$Q$          Q-criterion

$U_\infty$          Freestream Velocity

$x_{fw}$          Tangent plane to freestream flow at the front wheel centreline

$x_{rw}$          Tagent plane to freestream flow at the rear wheel centreline

$y^+$          non-dimensional height of the first cell from the wall

BOI          Body of Influence

CFD          Computational Fluid Dynamics

Coupled      Pressure-Velocity coupled algorithm based solver

GCI          Grid Convergence Index

LES          Large Eddy Simulation

RANS         Reynolds-Averaged Navier-Stokes

SIMPLEC      Semi-Implicit Method for Pressure Linked Equations-Consistent

URANS        Unsteady Reynolds-Averaged Navier-Stokes

# Chapter 1

# Introduction

Aerodynamic performance is an increasingly important part of passenger vehicle design. It can be optimised to reduce vehicle drag force in order to increase vehicle efficiency and range [1]. Design strategies have seen a consistent decrease in drag with some modern passenger vehicles boasting $C_D$ as low as 0.22 (figure 1.1). Aerodynamic drag is typically the largest resistive force for all automobiles, with smaller vehicles typically experiencing more drag than rolling resistance from speeds of 50km/h [1]. Gains in fuel efficiency have been observed in passenger vehicles as a result of reducing aerodynamic drag (figure 1.2) [1].

Image has been removed as it contains copyright material.

Image has been removed as it contains copyright material.

Figure 1.2: Fuel consumption against drag for a Mercedes-Benz B-class [1]

Figure 1.1: Vehicle drag coefficient decrease with respect to time with new data superimposed [1]

Wheel aerodynamics are an area of significant, ongoing research interest, typically contributing more than 30% of a vehicle's total drag [2–4]. Flow phenomena concerning isolated wheels have been investigated extensively while generic wheelhouse flows more relevant to passenger vehicles have not received the same attention in literature. The effects of the surrounding geometry on wheelhouse flows including any variations in wheelbase or overhang (the length a road vehicle extends beyond the wheelbase at the front or rear) have been studied to an even lesser extent. Many flow features differ due to wheelhouse geometry, generating distinct key flow structures that are in-turn influenced by the surrounding geometry (figure 1.3). Qualitative research modifying the wheel geometry or introducing passive flow injection into the front wheelhouse to manipulate

1

the wheelhouse flow field often did not consider the impact on the rear wheelhouse [4].
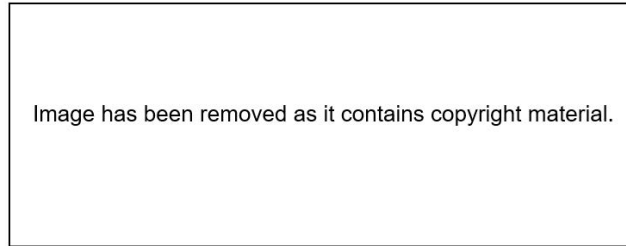


Figure 1.3: Wheel and wheelhouse vortices visualised in wet weather differ greatly to an isolated wheel case. Image from [5]

The industry emphasis on greater vehicle efficiency - in particular around aerodynamic drag force reduction, being a key theme in the development of electric vehicles - provides motivation and context for the current study. A study using a generic body with front and rear wheels is proposed where the wheelbase, front and rear overhangs may be varied in order to further the understanding around the interaction of flows concerning the front wheelhouse. This will allow for investigations into the flow interaction between the front and rear wheel for various wheel spacings, and the effects of both wheelhouses on the body.

# Chapter 2

# Literature Review

## 2.1 Wheelhouse Aerodynamics

Flows around wheels within a wheelhouse are observed to produce unique key flow structures due to the interaction of the rotating wheel and surrounding geometry. Flow enters the wheelhouse through the underbody, rolling up into a vortex denoted by H (figure 2.1), extending through the inner wheelhouse to generate vortices A and B. Vortex E is generated from the underbody flow expanding into the rear of the wheelhouse then interacting with the inner shoulder of the wheel before being drawn back into the underbody downstream. Vortices C and S are formed by the outer wheelhouse edge due to difference between flow velocity within the wheelhouse and freestream. Jetting vortices L and R are generated at the wheel-ground contact patch with the outboard vortex L being much larger and stronger than its inboard counterpart [6–8]. These characteristic flow structures introduce significant aerodynamic effects on the flow field surrounding the body [2, 9]. As such, many generic bodies have been evaluated experimentally, each with unique flow features that are influenced by the addition of rotating wheels [2, 6, 9–12]. The simplest of these was proposed by Fabijanic, an Ahmed-style body without the characteristic backlight, ground posts removed and replaced with a single set of wheels and wheelhouse (figure 2.2) [6].
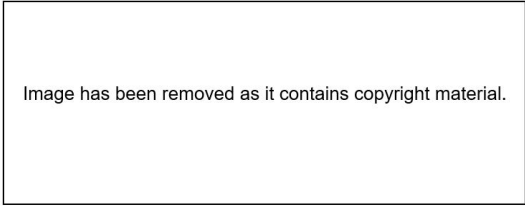


Image has been removed as it contains copyright material.

Figure 2.1: Generalised vortex skeleton of wheelhouse flow structures produced by Regert and Lajos using URANS [13]

Fabijanic observed unsteady, random flow fluctuating between inflow and outflow towards the rear

and lower edges of the wheelhouse [6]. Underbody flows upstream of the wheel were identified as the primary source of inflow into the wheelhouse with inner wheelhouse pressures varying with the change in forebody (front overhang) length which in turn would vary the yaw magnitude of the inflow [1, 6, 14]. Positive pressure at the front of the wheelhouse was observed with the remainder subject to negative pressures. It was determined that body lift and drag forces were more dependent on changes in radius and depth of the wheelhouse rather than volume [6].

Image has been removed as it contains copyright material.
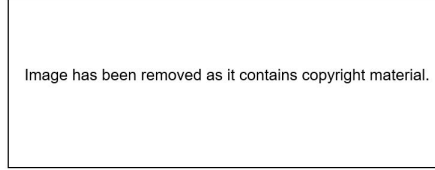
Figure 2.2: Fabijanic body as modelled by Krajnović and Fernandes [4]

Skea, Bullen, and Qiao differed in their geometry as the wheel was only shrouded across the top surface with both sides exposed to freestream flow [8]. Pressure distribution changes across the centreline were observed between the isolated and shrouded wheel, and varying ground conditions with lower negative peak pressures observed in the shrouded case caused by a change in oncoming flow [8]. The authors did not report the pressure distribution from within the wheelhouse but noted the potential transient nature of the flow at the rear of the wheelhouse [8] in agreement with the earlier studies [6]. It was also speculated that the rear wheelhouse flow field would influence drag by interfering with the base wake of the body but was not further investigated [8].

Regert and Lajos replicated the work of Fabijanic using numerical methods (RANS) and a body of different geometry, focusing on identifying a more detailed flow structure [3]. They identified that the flow field of an isolated rotating wheel with a moving ground plane offered little representation of flow structures within a wheelhouse with only the jetting vortices common between the two cases. Interactions between wheelhouse flows and those around the body were observed, vortices from the inner wheelhouse propagated into the underbody and contributed to the base wake while vortices from the top of the wheelhouse would flow out before merging with the wake at the rear (figure 2.3). Regert and Lajos had also investigated the impact of wheel position on the body as a function of wheel diameter from the rear face. The results published found that higher overall drag was experienced as the distance between the front face and the wheel was reduced [3]. A

4

key spacing of 1.5 wheel diameters for front overhang length from the forward face produced the lowest drag. Any variation in overhang length from this value would see overall drag begin to increase however no flow structures were identified as the mechanism for this change in force. In addition, forces were not evaluated as individual components to provide insight whether the wheel, wheelhouse or body contributed greatest to the drag variation observed, nor were flow feature responsible for the force variations identified.



(a) Vortex Skeleton on the short body
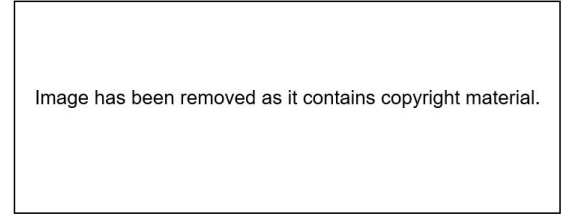


(b) Total pressure distribution behind the body

Figure 2.3: Flow features from Regert and Lajos first body [3]

Regert and Lajos continued their earlier work confirming observations of Fabijanic with wheel and wheelhouse geometry now more representative of the Fabijanic body [13]. Variations of the body were tested where the front overhang of $1d$ and $2d$ were investigated. It was confirmed that the wheelhouse inflow would yaw depending on the length of the overhang with the shorter lengths would significantly affect incoming flow angularity [6, 13, 14]. In comparison to the experiment [6], the numerical model produced similar trends but the drag forces were over-predicted (figure 2.4a). However drag for a $D/d = 1.4$ was under-predicted and the results of $D/d = 1.6$ from the previous experiments were not offered for comparison. Regert and Lajos also validated changes in wheelhouse depth produced little variation in overall drag (figure 2.4b), but would still contribute to an increase in lift [6, 13]. The authors also simulated a body with infinite length to isolate the effects of the wheel and wheelhouse. Although a small flow yaw angle was observed, no further effects on the flow field were presented. Wheelhouse inflow of the infinite front overhang case would still be subject to a small yaw angle. In addition, a minor discrepancy was noticed with the experimental radius data presented by Regert and Lajos, as Fabijanic had tested wheel-wheelhouse diameter ratios of 1.14 and 1.37 but were presented as 1.1 and 1.4 respectively and the 1.6 point omitted.

(a) Coefficient change for wheelhouse radius



(b) Coefficient change for wheelhouse depth
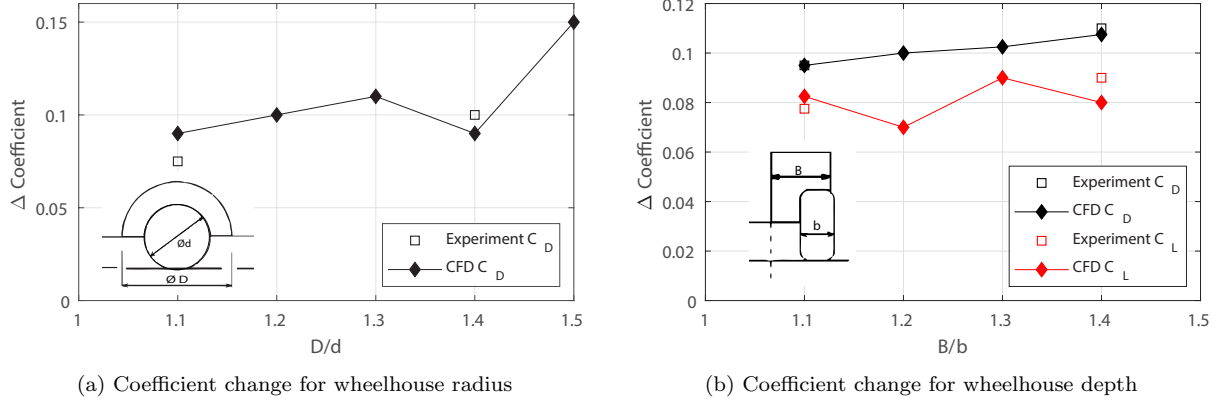
Figure 2.4: Wheel-Wheelhouse flow changes recreated with data from Regert and Lajos [13] and Fabijanic [6]

Regert and Lajos suggested that vortex H (figures 2.1, 2.5) moves outboard and combines with the wheelhouse edge separation to form the vortex C [13]. They also linked the front overhang length to the intensity of the Vortices A and B while the other vortices (H, C, E and the jetting vortices) showed little change however no quantitative or qualitative data was presented for comparison to support these findings. It was later confirmed through a LES study that the A and B vortices are extensions of the H vortex [15], suggesting that the vortex H is in fact dependant on the flow into the front region of the inner wheelhouse. This may be the case for the other vortices claimed to not be dependant on the front overhang length and leaves vortex C to form solely from the forward edge of the wheelhouse.



Image has been removed as it contains copyright material.
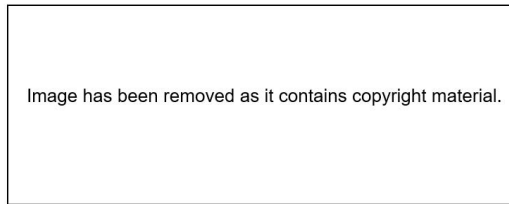
Figure 2.5: Vortex skeleton produced from time averaged LES with timestep $5 \times 10^{-4}s$ by Krajnović, Sarmast, and Basara [16]

A LES study on the geometry used by Fabijanic was conducted by Krajnović, Sarmast, and Basara and compared against previous experiments [6, 13]. The flow structures were in agreement with both studies with the exception of the $L_1$ and $R_1$ vortices reported as new findings (figure 2.5) [16]. Krajnović, Sarmast, and Basara identified variation between the wheelhouse pressure predicted

6

relative to the experimental results but were unable to identify the cause. They suspected it was a result of an unknown discrepancy between the experimental and numerical setup. $L_1$ and $R_1$ are formed by the flow being lifted from the ground plane and rolling up with the wheel rotation [16]. Both vortices are counter-rotating with respect to $L$ and $R$ and dissipate a short distance past the wheel as they were not observed further downstream. It is suspected that these small vortices may not have been captured in previous literature due to a lack of grid resolution at the wheel-ground contact. The instantaneous results modelled demonstrated the complex nature of flows within the wheelhouse. Additional evaluation of the downstream wake (figure 2.6b) shows the jetting vortex L and inner wheelhouse vortex E continuing downstream and along the body, with E remaining beneath the underbody.

Image has been removed as it contains copyright material.

Image has been removed as it contains copyright material.

(a)

(b)
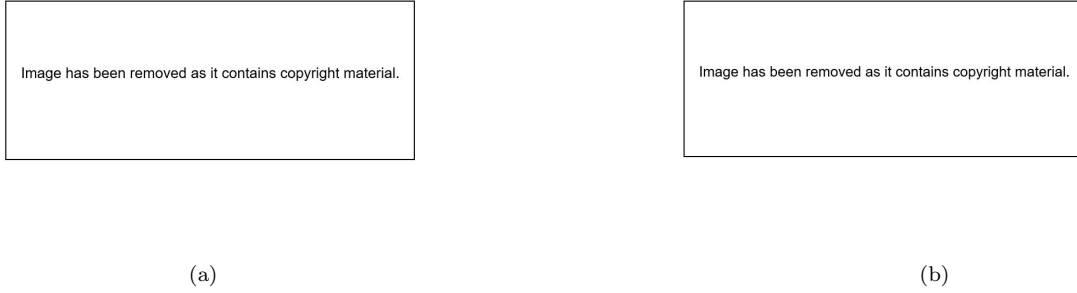
Figure 2.6: Flow visualisation produced from simulation by Krajnović, Sarmast, and Basara [16] of a Fabijanic body. (a) within and adjacent to the wheelhouse; (b) downstream of the wheel

Régert, Schwarczkopf, and Lajos modified an Ahmed body by adding a set of front and rear wheels based on the dimensional proportions from a previous study [11, 17]. The study was provided as an extension on previous work with the Fabijanic body as the Ahmed body could generate salient flow phenomena more typically representative of a passenger vehicle, namely the C-pillar vortices generated from the backlight. The addition of the rear wheels to the Ahmed body were reported to increase the width of the wake slightly, but no further description of the flow structures was provided. It was found that the base drag of the body had slightly increased when integrating pressure across the rear surface, however the 24% increase in drag was wholly attributed to the pressure acting on the wheels and wheelhouses. Lift increased over 40% as the wheel rotation affected the flow field under the body. Though a significant increase in drag was observed by the addition of the wheels it was lower than the 30% that would be expected from other investigations [2–4]. This could be due to the change in vortex C (figure 2.1) as the lower edge radius of the Ahmed body is larger than the Fabijanic body or another potential flow structure interaction

that was not investigated. The authors also determined that from their previous work [13] that while the flow field was unsteady, it was not categorised by large-scale unsteadiness and resulted in a quasi-steady flow [11], suggesting that a RANS CFD model is capable of reproducing the time-averaged flow features associated with a wheel within a wheelhouse.

Numerical investigations using the modified Ahmed body continued with Schwarczkopf, Regert, and Lajos for various wheel configurations and baffles placed upstream of the wheelhouse to manipulate the flow field [18]. Similar baffles had been evaluated experimentally by Dimitriou and Klussmann on a 1:2 scale BMW Z4 where the baffles would direct the air down and around the wheels resulting in a lower stagnation point on the wheel [19]. The baffle was positioned tangent to the oncoming flow, produced a vortex along the outer face of the wheel inducing lower static pressure at the front of the wheel. This resulted in a lower pressure distribution across the wheel centreline along with a 35% reduction in drag force [19]. The numerical results [18] with the baffle, tested in line with coming flow and at small yaw angles to oncoming flow, did not show major change to the flow field with only a minor drag reduction observed. The authors noted that baffles were not optimised and were identified as an area for further work. More significantly, changes to the front wheel geometry affected rear wheelhouse flows, resulting in notable change in drag force although no qualitative or quantitative assessment was offered for the rear wheel flow structures. In the case of Schwarczkopf, Regert, and Lajos, a reduction in drag was observed [18], reaffirming the need to further the understanding of the interaction between multiple wheels on a body. More recently a PIV study on the modified Ahmed body by Gulyás *et al.* observed significant outwash from the lower rear section of the front wheelhouse [20]. Flow features were only captured in the top-down and spanwise planes outboard of the front wheel and any effects at the rear wheel were not discussed.

Wind tunnel experiments performed by Bonitz, Larsson, and Sebben on a full-scale Volvo S60 at various yaw angles demonstrated wheelhouse flows in crosswind conditions [21]. The left hand front quarter panel and door was fitted with pressure sensors and a blanked-off wheel served to simulate a simple wheel case. A zero-yaw baseline case captured periodicity from wheelhouse vortex flows, in particular the S vortex (figure 2.5) shedding towards the upper radius of the wheelhouse. When subjected to crosswind conditions, the leeward side exhibited a much larger oscillating flow region extending towards to the lower half of the wheelhouse while the windward side showed little to no oscillations. The authors suggesting that relevant flows were directed into the vehicle underbody.

It can be determined that much research has gone into understanding the flow of the front wheel and wheelhouse however a lack of quantitative information exists for some flow key structures. It can also be said that the flow field around the rear wheelhouse may be less understood and has not received adequate attention, despite numerous studies introducing a rear wheel to their geometry. Many of the above authors have demonstrated that a change in the flow field is evident when a wheel is introduced to a body and further research around a geometry with a rear wheel is required to enhance the understanding of the flow field surrounding road vehicles [2].

## 2.2 Tandem Body Aerodynamics

Front and rear wheels on most automobiles are located in a tandem configuration relative to each other. Specific studies of wheels within a wheelhouse in tandem configuration are uncommon in literature. Cylinders in tandem configurations are the closest studies in literature however produce some significant limitations that are addressed in the following text. Placing bodies in a tandem configuration provides a drag reduction across both bodies as a function of their spacing (figure 2.7b) [22–25]. This interference between the two bodies sees the drag of the trailing body reduced from its freestream values as the boundary layer of the trailing body is tripped into a turbulent state due to the vortex shedding from leading body, even generating thrust for some small separations [22]. The most relevant literature has generally focused on two-dimensional studies or cylinders with large aspect ratio's [25].



Image has been removed as it contains copyright material.
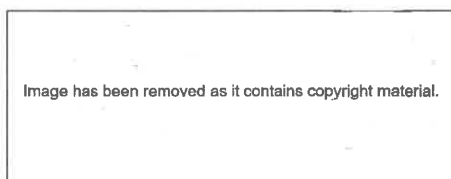
(a) Flow patterns of two cylinders in Tandem [25], adapted from [26]



Image has been removed as it contains copyright material.
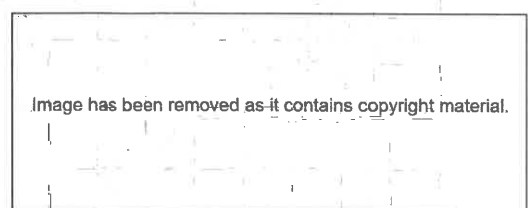
(b) Effect of drag due to space between two circular bluff bodies by Schuetz [1], adapted from Hoerner [22]

Figure 2.7: Effect on flow structures and drag on cylinder spacing

Exposed tandem wheels were investigated by Spagnolo *et al.* for small $X/D$ ratios (figure 2.7b) and different operating angles in a three dimensional case [27]. The effect wheel spacing has on both

9

wheels was documented to be caused by laminar-turbulent transition and interaction of vortices detaching from the front wheel shoulder and interacting with the rear wheel [27]. Interestingly the rear wheel in the study is observed to have a higher drag coefficient than the front wheel for each tested variation [28]. Such phenomena is a result for extremely small $X/D$ ratios [25] which may not be representative of automotive applications. A more recent numerical study on two Fackrell wheels in contact with the ground was performed with a wheel spacing of $0.5d$ [29]. Simulations were validated against past experiments [30] with drag being over-predicted by 6% and lift significantly more. Rear wheel drag was 33% lower than the front wheel as expected however it is difficult to verify the whether the boundary layer was sufficiently resolved as the presented images did not demonstrate adequate resolution. Only a brief comparison of the vortex cores between the single and tandem wheels was presented with no insight into how key flow structures are affected by the tandem wheel. To this authors knowledge, no further investigations into wheel spacing in automotive applications has been conducted.

## 2.3  Wheel-Ground Interaction Modelling

### 2.3.1  Wheel-Ground Contact Representation

Previous studies have identified the jetting vortices (L, R) generated at the wheel-ground contact patch as critical for replicating the flow field within a wheelhouse [2, 9]. This jetting is a result of the high pressure gradient observed at the contact point and the flow must change trajectory, forming the vortex on the outer lower edges of the wheel [10, 30]. Studies on isolated wheels have demonstrated how the wheel-ground contact is a sensitive parameter that can significantly influence the formation of the equivalent vortices [31] with inaccurate representation producing misleading results [10].

Cogotti stressed the importance of wheel rotation and effect of the contact patch during wind tunnel experiments [10] as the flow field differed between stationary and rotating wheels [2] in an attempt to achieve realistic test conditions. A block was proposed to simulate the contact between wheel and ground by allowing for rotation to be applied to the wheel from an external power source [10]. Despite these attempts, the ground plane in the study was still stationary and the large block used is anticipated to compromise the formation of the critical L and R (jetting) vortices. Most wheel
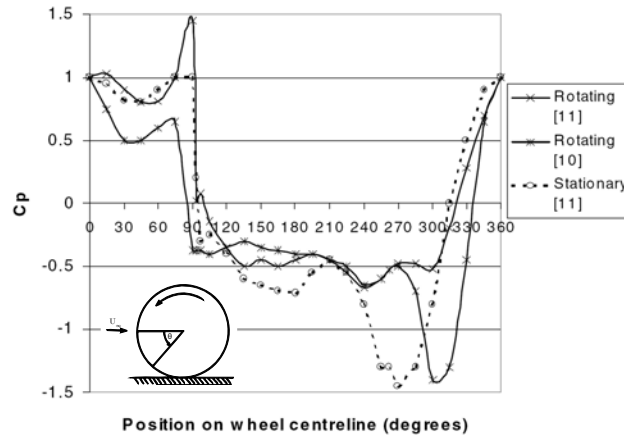
Figure 2.8: Pressure Coefficient plot across wheel centreline. Original data from [8, 30, 32]

studies since Fackrell and Cogotti have included moving ground planes for accurate representation of jetting vortices which were commonly performed with a slick wheel (figure 2.9). This led to further investigation of the wheel-contact interface by Dimitriou and Klussmann, where tyre tread and interaction with an open-wheel car were introduced [19]. Their results were in agreement with Fackrell however the stagnation pressure magnitude that contributes to the jetting vortex did not match previous studies. Small openings provided by the tyre tread allowed for air to pass through the contact region, effectively reducing stagnation pressure at the contact patch [19]. The second part of the study also identified that surrounding geometry influences the flow field around the wheels demonstrating distinct differences between open and closed wheel vehicles.

Image has been removed as it contains copyright material.

Image has been removed as it contains copyright material.
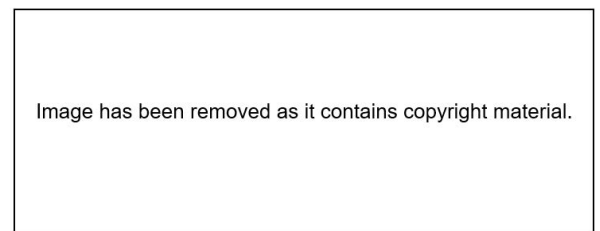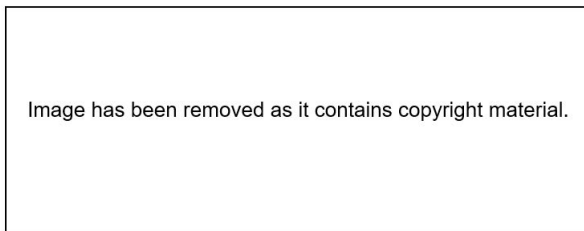
(a) Schematic of rotation behind an isolated wheel [31]

(b) Numerical streamline behind an isolated wheel with moving ground [9]

Figure 2.9: Isolated wheel flows

Accurate numerical representation of the contact region is an extremely challenging and critical region to discretise using finite volume methods as the wheel contact is tangent to the ground [31].

Inadequate modelling of this region can lead to negative volume cells, increasing the likelihood of highly skewed elements being formed unless methods such as submerging the wheel into the ground plane are implemented to mitigate the issue. Comparable numerical results to an experimental setup were achieved with a wheel in contact with a moving ground [33], where the lower face of the tyre was trimmed between $80^o$ and $100^o$ then a vertical wall extruded downwards to the ground plane. This presented itself as an alternate method to resolving the wheel-ground contact, allowing for better quality mesh generation and boundary layer modelling.


Image has been removed as it contains copyright material.
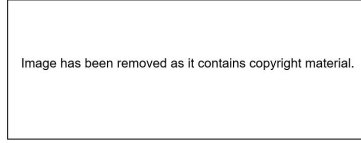
Figure 2.10: Unstructured mesh around the contact patch [18]

Schwarczkopf, Regert, and Lajos had submerged the wheel into the ground for their study (figure 2.10), employing a $y^+ > 30$ for boundary layer modelling and ignoring prisms in at the contact region [18]. Wall resolution against their base case without wheels was in agreement with previous experimental results [18] but was not reconfirmed with wheels. A wheel submerged into the ground plane may reduce the chance of highly skewed cells being generated but introduced additional complications. The lack of wall resolution at the wheel-ground contact leads to a change in pressure across the wheel and contact patch further affecting the vortex structures generated by the wheel [31].

### 2.3.2 Ground Representation

A significant portion of research on wheelhouse flows concerns moving ground plane effects. Numerous authors have studied such effects on an isolated wheel with subsequent evaluations involving wheelhouse flows [2, 8, 9]. Experimental evaluations showed that the moving ground condition influenced the lift and drag forces significantly on passenger cars [2]. Elofsson and Bannister noted the potential specificity of their results as the study was conducted on a Volvo S40 rather than a generic form, however further experimental evaluations of a modified Ahmed body with wheels and another with a geometrically altered Fabijanic model were both still conducted without a moving ground [20, 34]. Both studies used a cut-out to to allow for the wheel to be lowered into the ground to simulate contact and allow the wheel to still rotate. While the test facilities may not have been

equipped with moving ground capabilities, such results need to be taken with consideration due to the potential change in flow field at the wheel-ground interface (figure 2.11) [2, 9, 10].





(a) Stationary ground
(b) Moving ground
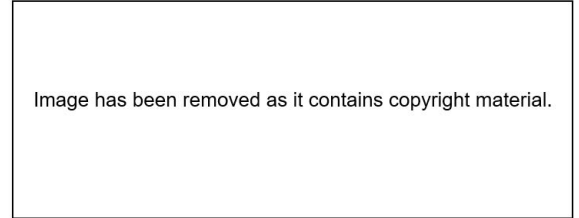
Figure 2.11: Numerical representation of vortices with different ground conditions [9]

Wäschle had also performed an extensive study of rotating wheel flows with changing wheel rim detail on a 1:4 scale simplified Mercedes-Benz E class both numerically and experimentally [9]. Boundary layer control with a moving ground was applied during the experimental case [35], allowing for investigation into the flow structures for both stationary and rotating conditions (figure 2.11). It was observed that the vortices generated by the wheel and wheelhouse were lower in position in the rotating wheel case and resulting near wake of the vehicle was somewhat narrower, which agrees broadly with findings of other investigations [2, 8, 16, 34].

Differences in flow features between the stationary and rotating wheels are significant where the stationary wheel produces a larger wake [2] while the jetting vortices are lower and interact differently with the moving ground plane [9]. Such studies conclusively indicate that rotating wheels in contact with a moving ground are critical to achieve representative flow structures of a wheel. Multiple authors [7, 8, 12] investigated other generic bodies and focused on effects between a rotating wheels within a wheelhouse with a moving ground plane, with all authors agreeing on the importance of rotating wheel and moving ground conditions to produce more realistic results from experimentation and simulation. The above authors however did not present any quantitative data from within the wheelhouse and only reporting overall force results or flow features outside the wheelhouse as the ground conditions changed.

## 2.4    Research Objectives

It is established that wheel and wheelhouse flows affect the surrounding flow field of a vehicle and make a significant contribution to vehicle drag. Key vortices generated by the wheel and wheelhouse are influenced by changes in wheelhouse-wheel diameter ratio and overhang. These flow structures are also extremely sensitive to change in modelling representation, with moving grounds and the wheel-ground contact interface significantly affecting experimental results. Most of the studies reviewed were primarily focused on bodies with a single wheel or on more specific bodies that had only reported on effects at the front wheel. A need for a generic model consisting of both front and rear wheels has been identified in order to study interactions between both wheels.

Therefore, the goals of this research are:

1. Establish a CFD model that uses an adapted reference body that will allow for modification and placement of a rear wheel and wheelhouse, positioned in a manner relevant to current automotive designs.

2. Investigate key flow structures and produce quantitative data for the front and rear wheels, and flow through the inner wheelhouse for varying wheel spacings on the reference body.

3. Determine the effects of an overhang change to the front and rear wheel flow structures for a fixed wheel spacing.

4. Investigate a combination of variations in front overhang and wheel spacing to establish the aerodynamic relationship between these parameters.

# Chapter 3

# Methodology

## 3.1 Geometry

### 3.1.1 Reference Body

Numerous reference models have appeared to examine characteristic flow features around passenger vehicles [36]. These models generally lack wheels, apart from the modified Ahmed model of Régert, Schwarczkopf, and Lajos, some reference bodies originally modified by Cogotti and the more recent DrivAer model [11, 36, 37]. Many of the flow features relevant to wheel studies have generally been related to more specific cases. Given the wealth of data that has been generated using the Fabijanic geometry both experimentally [13] and numerically [4] this study will also utilise this geometry.



(a) Modified Fabijanic body with front and rear wheels

(b) Test body within fluid domain
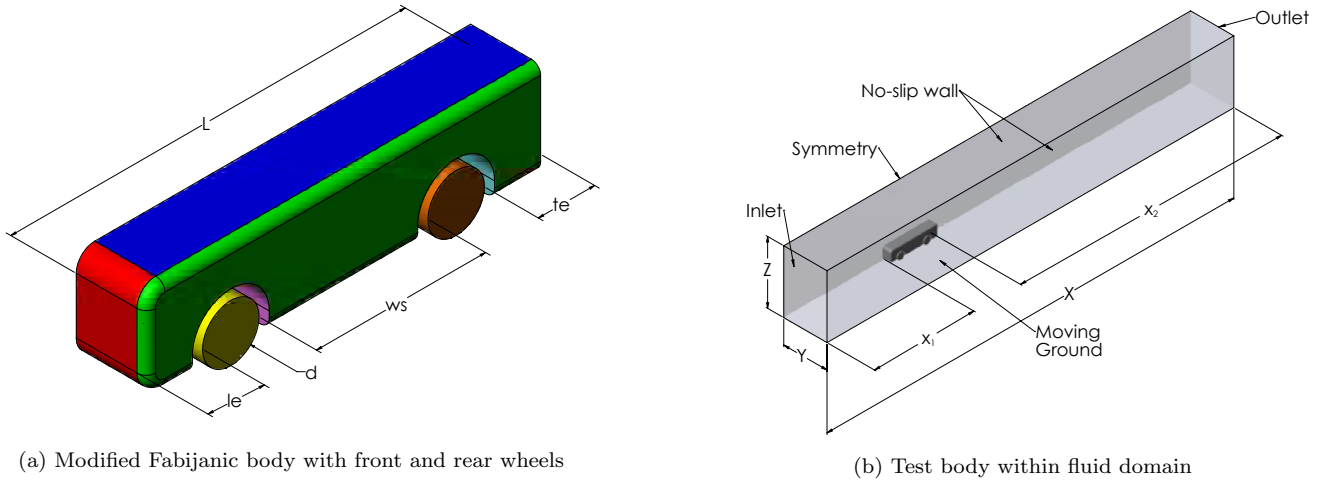
Figure 3.1: Test geometry and fluid domain

The geometry (figure 3.1a) has been modified from Fabijanic (figure 2.2) to include a second, rearward wheel and wheelhouse. Leading and trailing edges dimensions, denoted by $le$ and $te$, are placed at $1d$ from the nearest vertical tangent plane to the wheel while wheel spacing ($ws$) is set at $3d$ for the baseline configuration. Wheel and wheelhouse width and diameter are sized based on the dimensions used by previous literature [4, 6, 13]. To understand the contribution that each

of the geometric features makes to the overall lift and drag, the body surfaces have been named individually as indicated by the various colours (figure 3.1a). A complete geometric description is provided in table 3.1.

| Dimensions in mm | | | | | | | | | | | |
|---|---|---|---|---|---|---|---|---|---|---|---|
| Body Dimensions | | | | | | | | Domain Dimensions | | | |
| H | 127 | ws | 229.8 | $r_{wh}$ | 52.3 | $d = le = te$ | 76.6 | X | $L + x_1 + x_2$ | $x_1$ | $8(H+h)$ |
| L | 536.2 | h | 16.8 | g | 14 | $r_2$ | 12.5 | Y | 500 | $x_2$ | $21(H+h)$ |
| W | 190.5 | $r_1$ | 25 | $w_{wh}$ | 50.5 | w | 36.2 | Z | 750 | | |

Table 3.1: Body and domain dimensions

### 3.1.2  Computational Domain

Domain dimensions for inlet and outlet distances were calculated as a function of the body's height, $H$, and ground clearance, $h$ (figure 3.1b) as per Krajnović and Fernandes [4]. These dimensions were deemed sufficient in previous studies of similar shaped bodies [38]. The height of the domain (Z) matched the wind tunnel and domain dimensions from previous studies [4, 6] however width (Y) was increased to reduce any near wall effects from the side of the domain and to allow for more stable mesh generation between the refinement boxes and far-field walls. This resulted in a blockage ratio of approximately 3.39%. Domains offering a lower blockage ratio (1.93% and 0.847%) were evaluated realising negligible changes in the body forces and relevant trends despite a computational resource penalty.

## 3.2  Boundary Conditions

Freestream velocity of $30m/s$ was applied to the inlet in conjunction with a moving ground translating at the same velocity (figure 3.1b) to match previous studies [4, 6, 13], providing a Reynold's Number of $1.11 \times 10^6$ based on body length. The body of the vehicle is represented as a no-slip wall and angular velocity of 783.2 rad/s applied to the wheels to ensure the tangential velocity of the wheel is consistent with the ground plane. Outlet reference pressure is set at zero gauge pressure, with the far-field walls set with a slip-wall condition and symmetry was applied at the centre plane. A comparison simulation was performed against previous studies [4, 6] with the far-field walls modelled with a no slip condition and near wall modelling applied. An additional study with inlet and outlet distances placed at double distance was conducted with no significant change in flow structures or body forces observed in the comparison studies.

## 3.3 Turbulence Modelling

The Realizable $k - \epsilon$ model was used for turbulence closure due to its suitability for resolving rotating shear flows [39] and has successfully been used in previous studies [11, 18, 40]. The $k - \omega \, SST$ model was also considered as per Regert and Lajos [13] and evaluated during initial studies (see figure 3.5 in section 3.7). However, it was found less suitable due to a greater variance in the forces, momentum and turbulence quantities. In addition, the Realizable $k - \epsilon$ model was capable of predicting forces closer to experimental values [11, 41] with the added benefit of producing a converged solution sooner. A comparison against experimental values and a comparable CFD study [13] that employed a coarser mesh and $k - \omega \, SST$ turbulence model can be found in section 3.7.

A sensitivity analysis varying turbulence intensity, $I_{uu}$, from 0.35% to 5% and axial length scale, $l$, between $0.07 D_H$ to $D_H$, was undertaken, revealing force variations less than 0.1%, minimal differences around wheel and wheelhouse flows with higher $I_{uu}$ limiting body separations. Inlet $I_{uu}$ was ultimately set to 0.35% consistent with the wind tunnel facility at Macquarie University [42] to facilitate as a comparison for future experiments, which is still lower than what would be experienced under real-world conditions [43]. Turbulent length scale was calculated from the domain's hydraulic diameter to yield $l = 0.042 m$ [44, 45].

### 3.3.1 Near Wall Modelling

A target $y^+ \approx 2.5$, corresponding with previous studies [40], with a first cell height of 0.03 mm grown 11 layers was implemented. This resulted in a total thickness of 1mm with a non-dimensional wall distance $y^+ \approx 100$. Plotting $y^+$ across the surface of the test body showed that the average $y+$ was lower than the target, with stagnation points on the front of the wheel and leading edge radius of the body having a $y^+ < 5$.

Predicted first cell height was tested down to $y^+ \approx 1.5$ with results varying by 0.1% and requiring a 7% increase in total cell count for each prism layer added. Enhanced Wall Treatment was applied to the turbulence model as the first cell height is well within the sub-viscous layer and prisms grown across all surfaces of the body and ground plane In addition, the turbulence model and wall treatment defined in the solver setup is uses the two-equation method in the fully turbulent
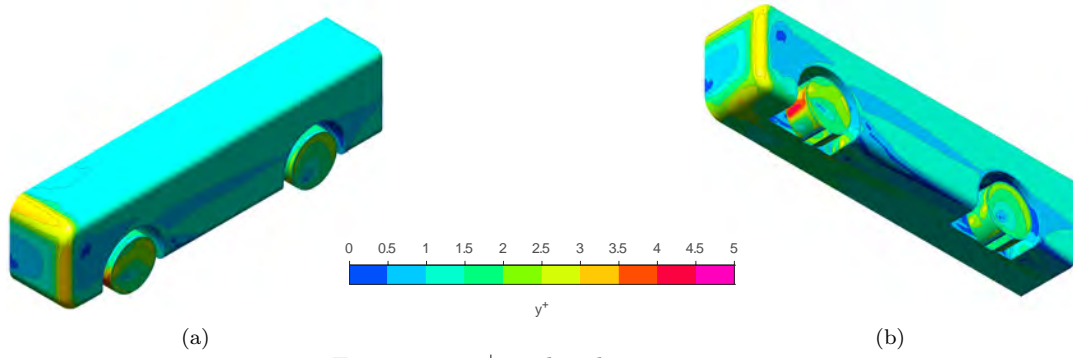
Figure 3.2: $y^+$ on baseline geometry

region ($y^+ > 200$) and was not needed to be grown further [45]. Growing the prism layers up to a $y^+ = 200$ introduced poor quality cells in the region surrounding the contact patch. Therefore prism layers were grown up to $y^+ = 100$ and adjoining refinement zones around the contact patch and wheels were refined sufficiently to allow for smooth transition between prisms and surrounding cells. This was deemed as a suitable compromise to improve cell quality and reduce mesh count, and allowed for a blending function for turbulent viscosity to be employed for outer region of the boundary layer [45].

## 3.4   Solution Initialization

The calculation was initialized with the solution from the Fabijanic body verification case that ran for 1000 iterations to reduce simulation time. Comparisons with the default hybrid initialization techniques in FLUENT found no significant variations in forces and flow structures while simulation time was halved. Relaxation factors were altered from their default values of 0.8 to 0.5 for pressure, and 0.5 to 0.2 for turbulent production and dissipation for the first 100 iterations to allow for any changes in the flow field to be established [45]. They were returned to their default values for the remaining iterations until convergence was reached.

## 3.5   Solution Convergence

Numerous studies were performed to determine convergence criteria. Flow in the region of interest is highly transient in nature as reflected by oscillations in the force plots across the wheel, wheelhouse and body. Initial runs with the SIMPLEC solvers with second-order numerical schemes to enhance numerical stability [39] were run for 5000 iterations, finding that with increasing mesh

density, required approximately 4,500 iterations before periodicity was reached in the force plots. These runs were continued for an additional 2,000-10,000 iterations depending on mesh density to confirm the oscillations were regular with less than 0.5% variance of body forces. The coupled solver was then implemented and produced stable periodicity much sooner in the simulation; between 200 and 400 iterations depending on mesh density and if any under-relaxation was applied. It was then only run for a total of 1,000 iterations to ensure a stable average could be taken. When comparing solve times, the coupled solver would yield results within 0.2% variance in half the time of the SIMPLEC solver and was the solution method used for the study. Final values were taken by averaging across a minimum of 3 the oscillations once they had reached periodicity for all quantities.

## 3.6   Mesh Description
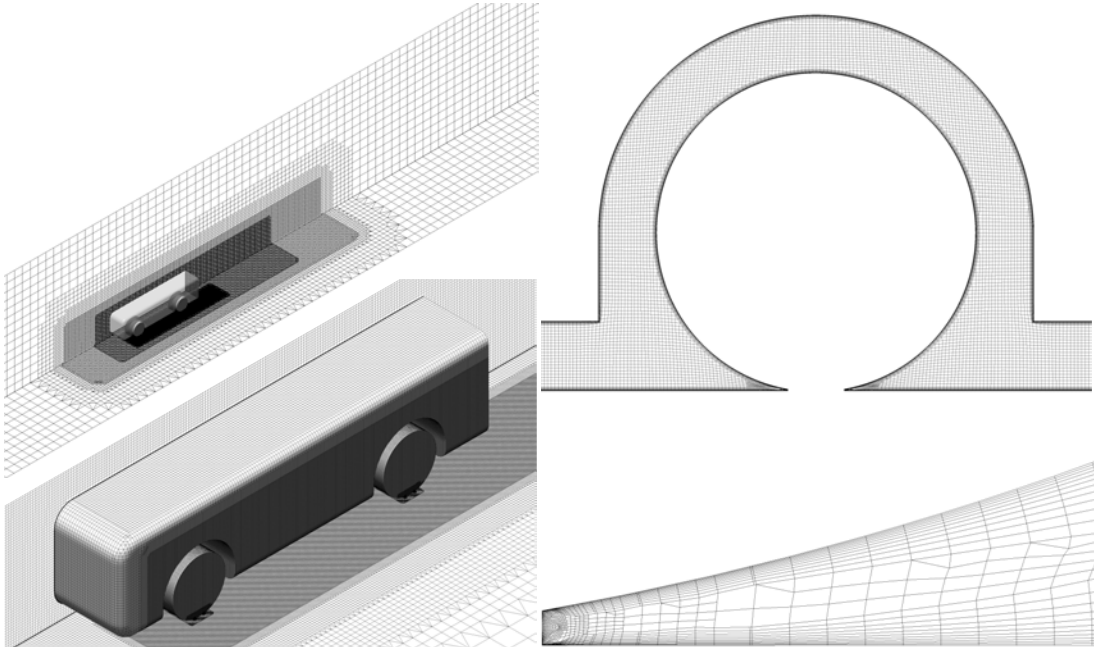


Figure 3.3: Top left - global mesh sizing; Bottom left - surface mesh of the test body; Top right - wheelhouse mesh through the centreplane of the wheel; Bottom right - contact mesh with prism layers

FLUENT was used for mesh generation to produce a cut-cell mesh (figure 3.3) consisting of predominately hexahedral elements. This meshing method was selected based on its ability to produce a higher quality mesh over a tetrahedral method with the added benefit of a reduced mesh count and solving time. Four refinement zones were placed around the test geometry to capture flow structures downstream and through the wheelhouse, resolve drag forces on the body and pressure

at the contact patch. The contact patch was modelled with a step height of $0.003d$ [31]. Some mesh smoothing was required to achieve a desired maximum skewness less than 0.98 and orthogonal quality greater than 0.02. Automatic node swapping and smoothing targeted poor-quality cells for improvement, resulting in a suitable mesh for solving. Final mesh size consisted of approximately 17 million elements.

| BOI | Contact | Wheelhouse | Body | Greater Refinement | Domain |
|---|---|---|---|---|---|
| Grid Level $n$ | 3 | 5 | 8 | 9 | 11 |

Table 3.2: Grid levels for each BOI and domain

### 3.6.1   Grid Verification

A range of mesh densities were applied to the domain and Bodies of Influence (BOI) around the geometry consistent with appropriate simulation of key flow structures. Preliminary simulations showed oscillations in the streamwise and spanwise residuals with turbulence quantities oscillating randomly for coarser meshes. Increased resolution eventually produced a solution with periodic oscillations that did not exceed 0.2% of the mean monitor forces. FLUENT calculates edge length as a function of the smallest defined edge with *edge length* $= 2^n \times$ *minimum size* [45] where $n$ is the grid level. The smallest edge was located at the wheel-contact contact and grown out to the boundaries with the sizing in table 3.2. Each change in size was given a buffer layer of 5 elements to account for any sudden variations in grid spacing (figure 3.3).



Figure 3.4: Convergence of force coefficients

Various minimum sizes (0.02mm to 0.06mm) were applied to produce a range of mesh densities and to determine the size for convergence against the experiments of Fabijanic [6]. Little variation was observed between the 9.8 million elements (minimum size = 0.0275 mm) and the finest case of

22.5 million elements (minimum size = 0.02mm). It was determined that any further refinement in mesh would not yield any materially significant increase in accuracy (figure 3.4).

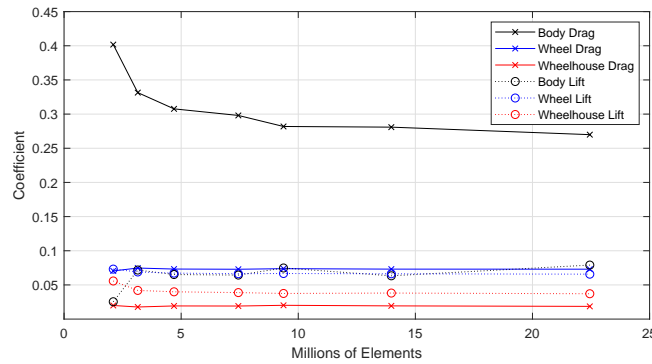| Surface | Relative Error | Error to Exact Solution | $GCI_{F_s=2}$ |
|---|---|---|---|
| Body Drag | 4.43% | 9.00% | 9.94% |
| Wheel Drag | 1.02% | 2.15% | 2.29% |
| Wheelhouse Drag | 8.36% | 16.36% | 18.78% |
| Body Lift | 5.40% | 10.80% | 13.08% |
| Wheel Lift | 1.50% | 3.25% | 3.63% |
| Wheelhouse Lift | 1.07% | 2.30% | 2.59% |

Table 3.3: Solution error between selected ($9.8 \times 10^6$ elements) and finest grid ($22.5 \times 10^6$ elements)

Grid Convergence Index (GCI) was calculated and compared with the exact solution using Richardson's extrapolation for the body and wheel forces [46]. The chosen grid produces conservative results against the finest grid solution, with a $F_s = 2$ against the exact solution defined by $f_{exact} \simeq f_1 + (f_1 - f_2)/(r^2 - 1)$ (table 3.3) [46]. The exact error is below 6% for the wheel forces and is assumed to be within the asymptotic region [46].

## 3.7  Validation

The sizing used for the 9.5 million element case (0.0275mm) was then applied to the different wheelhouse diameters as tested by Fabijanic and compared in figure 3.5. The simulation model was capable of producing excellent results for the 1.37 and 1.6 wheelhouse ratio cases and are in very good agreement with the experiment [6], a significant improvement over a previous comparable CFD study [13]. These results are reflective of the turbulence model and contact modelling method chosen in this study. Drag for the 1.14 case has been over-predicted, it is suspected that the smaller wheelhouse ratio requires further refinement to accurately resolve the flow field within the wheelhouse. This case was not further investigated as this configuration was not evaluated in the study. Results for the $k - \omega SST$ comparison simulations are also presented and did not predict the same trend as the experiment by Fabijanic or Realizable $k - \epsilon$ turbulence model.

Detailed inner wheelhouse flow structures obtained in the verification case were compared against previous LES simulations (figure 3.6) [15, 16] as they had not been measured in previous experimental studies of this geometry. Key flow structures E, H and R have been captured in similar locations to the previous studies (figure 3.6b). A key observation between these flow structures is that a suitable RANS model is capable of capturing comparable flow features against time-
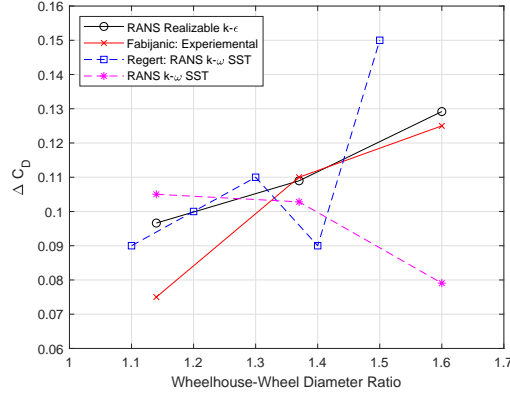
Figure 3.5: Comparison to published results [6, 13]

averaged LES results using substantially less computational resource. The RANS model produced these results in 2.6% of the time required when compared to LES simulations of similar grid densities and computational resource [15]. Differences in geometric setup were noticed as the previous studies submerged the wheel into the ground plane which can affect vortex formations around the wheel. In addition, the geometry setup in figure 3.6b was presented with a longer overhang to the geometry in this study and previous literature, further affecting the formation of key flow structures.



(a) Inner wheelhouse flow structures presented by Krajnović, Sarmast, and Basara [16]
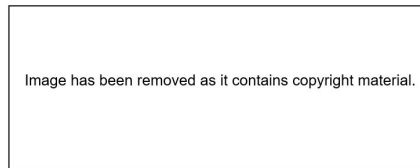


(b) Inner wheelhouse flow structures presented by Viswanathan [15]
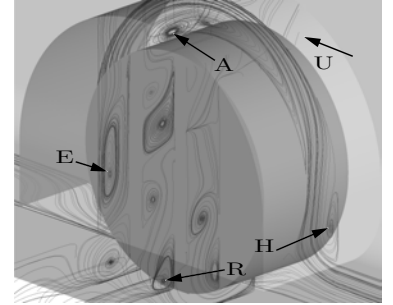


(c) Inner wheelhouse flow structures from the verification case

Figure 3.6: Comparison of flow structures within the inner wheelhouse for a single wheel body

### 3.7.1 Computing Resource

Simulations were conducted on a server consisting of two Intel Xeon processors each with 18 physical cores with 2.3GHz base clock speed and 128GB of RAM. No GPU acceleration was implemented. Approximate solution time was 11 hours per 1000 iterations at $10 \times 10^6$ elements.

# Chapter 4

# Results and Discussions

Significant differences occur in key flow structures with changes to wheel spacing and geometry overhang, varying from minor spatial displacement and magnitude to a greatly varied flow field that suppresses the formation of other flow structures downstream. Each geometric change presents unique flow conditions producing unique overall force trends. The cases presented here focus on geometrical changes that significantly impacted the flow structures and forces on the body. Wheel spacing was varied with respect to wheel diameter ($ws/d$) for a broad range of cases that may be found in automotive applications. Front and rear overhang was then varied on a fixed wheel spacing of $ws/d = 3$ to establish how the change in flow structures at the front wheel would affect the tandem wheel downstream. The varying wheel spacing study was repeated for the new front overhang cases to demonstrate whether flow structures at the rear wheel and wheelhouse are dependant on the geometry upstream. Iso-surfaces were plotted with Q-criterion ($Q$) to follow the vortex cores downstream and monitor their interaction with the wheel, wheelhouse and any other downstream flow structures. Transparency ($\alpha$) was also applied to observe any other flow structures that may be obscured by the geometry or larger vortex, namely the large separation at the front lower shoulder of the front wheel. In addition, the vortex naming convention is in line with previous studies [13, 16].

## 4.1 Effects of Variations in Wheel Spacing

Wheel spacing, $ws$, was varied along with the body length $L$ for this component of the study while front and rear overhangs were fixed, $le = te = d$, (figure 3.1a). Front overhang was held constant to isolate the effects of adding a tandem to a geometry with varying length. Results indicated body drag increased with body length for both geometries however the minimum forces did not occur at the shortest geometry for the tandem wheel body (figure 4.1). A drag force minimum was observed for wheel spacing $ws/d = 1.5$ and lift force minimum at $ws/d = 2.0$ before forces begin to increase. It was inferred that the rear wheel and wheelhouse must have a significant influence

(a) $C_D$  (b) $C_L$
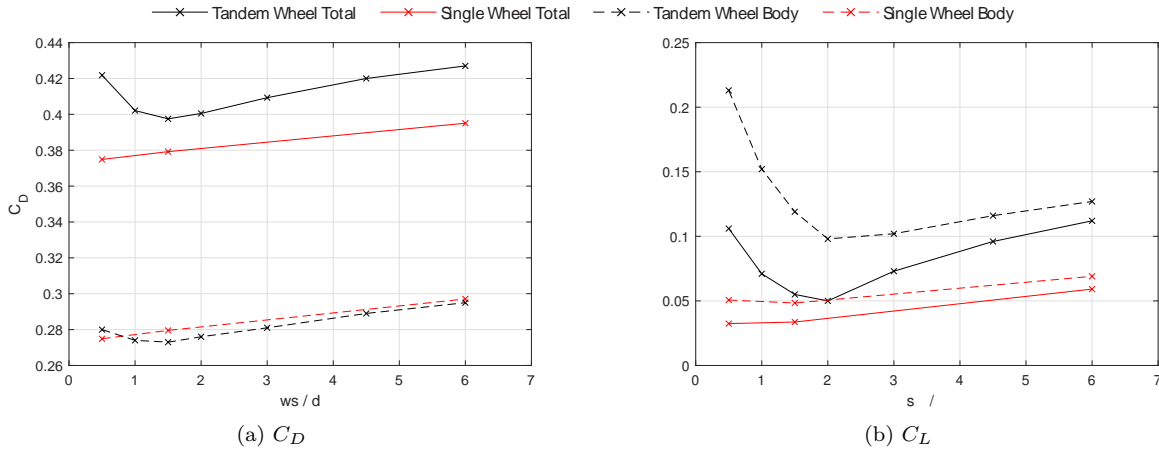
Figure 4.1: Force coefficient change between single and tandem wheel bodies

on the surrounding flow field to generate this change in force on the body.



(a) $C_D$  (b) $C_L$
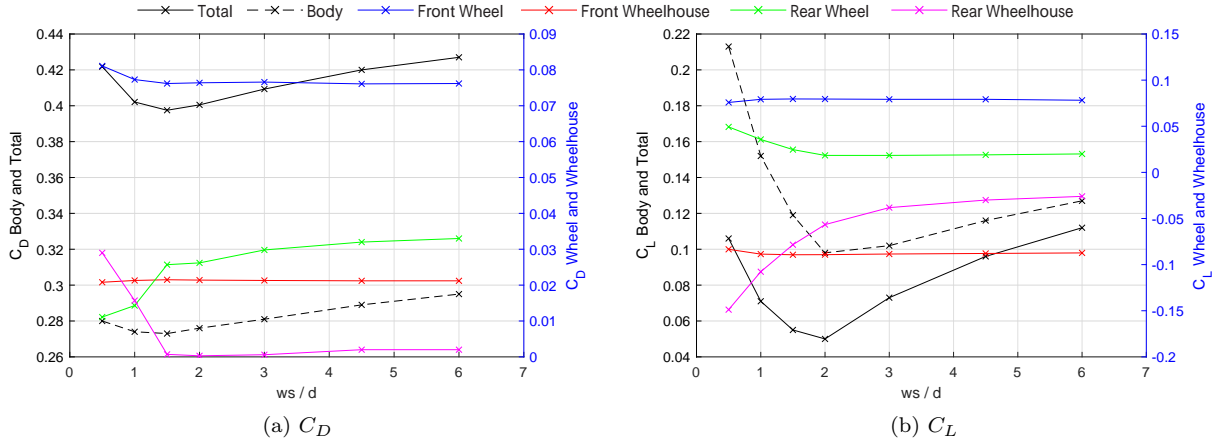
Figure 4.2: Force coefficient change for baseline overhang

The wheel and wheelhouse forces were monitored on the tandem wheel body individually to establish where the most significant change occurred (figure 4.2). Front wheel and wheelhouse produced broadly linear trends for lift and drag with a notable drag increase from $ws/d = 1$ while changes at the rear wheel and wheelhouse showed more considerable changes. Rear wheel drag decreases from $ws/d \leq 1.5$ however the most significant change occurs with the large increase in rear wheelhouse drag. Similar observations are made with respect to lift at the rear wheel and wheelhouse where substantial force changes occur.

### 4.1.1 Front Wheel Flowfield

The investigation revealed changes in front wheel flows with varying proximity of the rear wheel. Vortex E, generated at the rear inner wheel shoulder (figure 4.3d-4.3f), no longer flows into the

underbody and instead is projected out of the wheelhouse in the spanwise direction. Vortex S on the upper rear edge of the wheelhouse forms and is drawn towards the outboard jetting vortex L for $ws/d = 1$ and is disrupted by the presence of the rear wheelhouse at $ws/d = 0.5$ (figures 4.3a-4.3c). Inner wheelhouse surface pressure is relatively consistent across all cases along with the vortex formations A, B and H still present and relatively unchanged (figure 4.3). Flow structures generated by the front wheel showed no distinctive change for wheel spacing $ws/d > 2$.



(a) $ws/d = 0.5$  (b) $ws/d = 1.0$  (c) $ws/d = 1.5$

(d) $ws/d = 0.5$  (e) $ws/d = 1.0$  (f) $ws/d = 1.5$

Figure 4.3: Vortex cores around the front wheel for varying wheel spacing with overhang $le/d = 1$, plotted with $Q = 3.2 \times 10^5 \ s^{-2}$, $\alpha = 0.45$

Flow features behind the front wheel are relatively consistent for each wheel spacing (figure 4.4). The outboard jetting vortex L has a prominent core for all cases however is in its weakest form for $ws/d = 1.5$. Vortex E is drawn towards vortex L for $ws/d < 1.5$ and creates a large region of lower total pressure compared to other cases (figures 4.4a, 4.4b), effectively increasing front wheel drag (figure 4.2a). This rotation is extended in the spanwise direction and eventually interacts with vortex L generated by the rear wheel (shown in section 4.1.2). The inboard jetting vortex R remains consistent across all cases and eventually dissipates before reaching the rear wheelhouse for cases $ws/d > 1.5$.

Flow structures in the wake of the front wheel are dependant on rear wheel positioning. Vortex
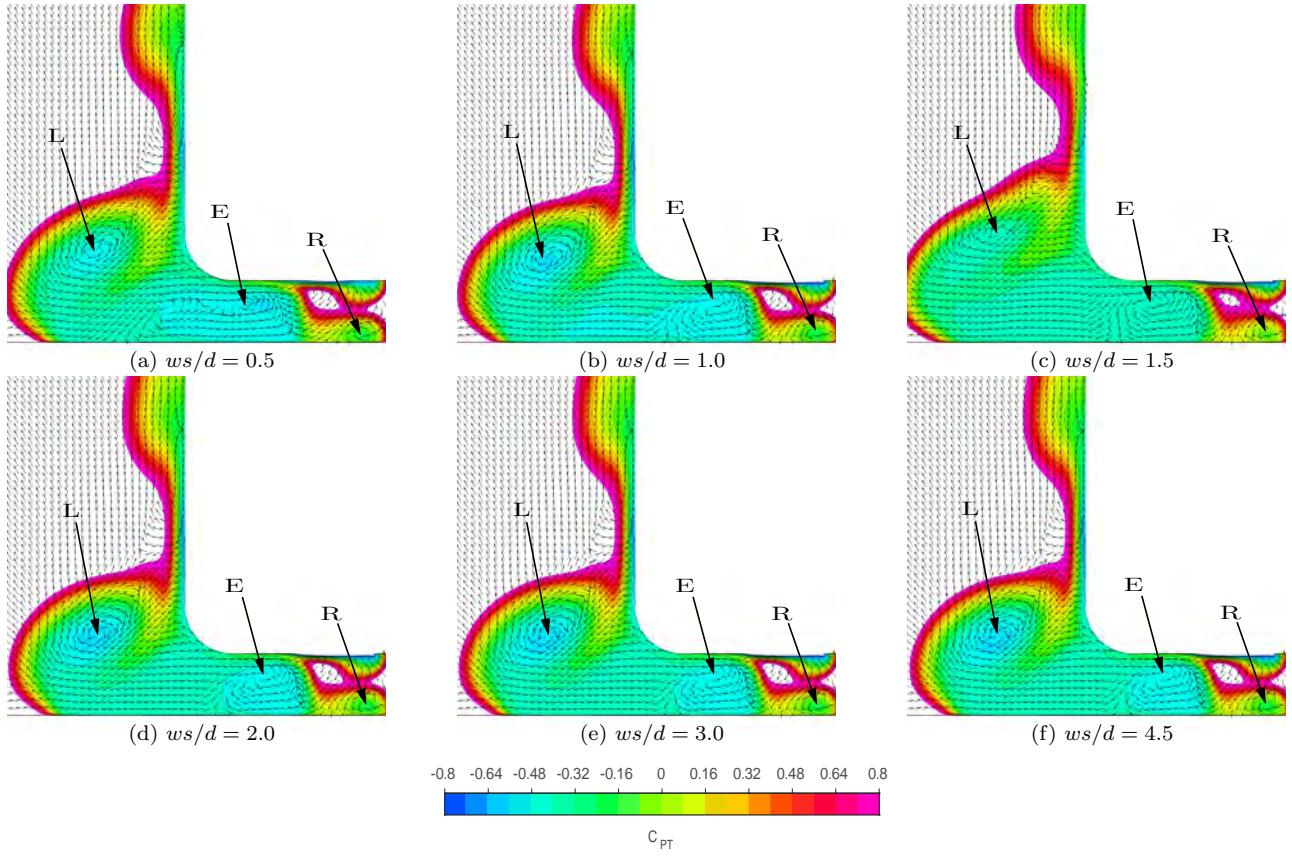
Figure 4.4: Front wheelhouse outflow for varying wheel spacing with overhang $le/d = 1$ at $x_{fw}/d = 0.69$
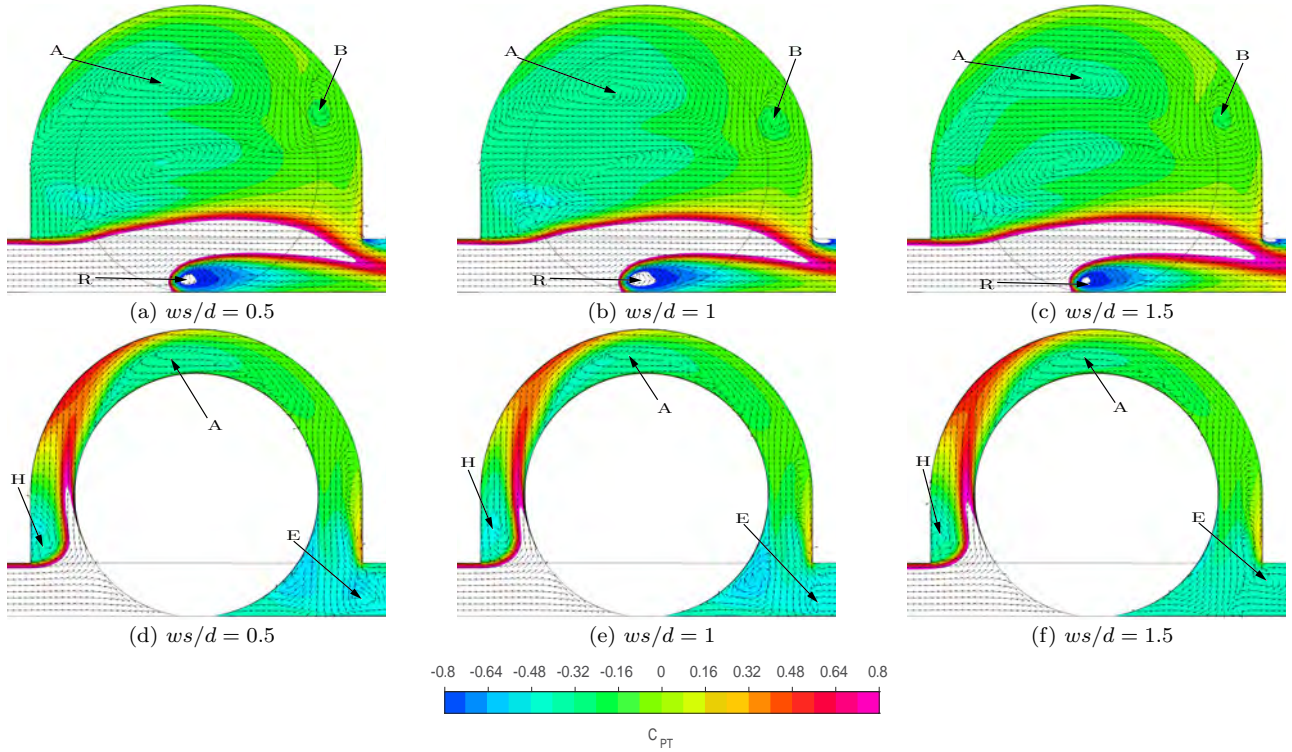


Figure 4.5: Front wheelhouse spanwise flow for varying wheel spacing with overhang $le/d = 1$; (a-c) $y/d = 0.68$; (d-f) Wheel midplane, $y/d = 1$

H remains consistent in each wheel spacing variation, and flow through the upper wheelhouse presented no distinct change in flow (figure 4.5). Flow direction in the wake of the front wheel is also dependant on the proximity of the rear wheel. Vortex E is extended downstream as the spacing is increased and promotes flow back into the rear wheelhouse. However for $ws/d = 1.5$ the rotation between the rear face of the wheel and vortex E is no longer present and is unique to this spacing (figure 4.5f). Coincidently, minimum drag occurs at a spacing of $ws/d = 1.5$ when this rotation is no longer present. Based on the front wheel flow field, the proximity of the rear wheel and wheelhouse have little effect on key flow features ahead of the front wheel but affect the outflow from the front wheelhouse, with vortex E being most sensitive to changes in wheel spacing. These changes in the flow field are responsible for the increases in front wheel drag and significantly affect the flow field around the rear wheel and wheelhouse, shown in the subsequent sections.

### 4.1.2 Rear Wheel Flowfield

Flow structures at the rear wheelhouse are significantly different than what was observed within the front wheel. The outboard jetting vortex L was most influenced by the wheel spacing $ws/d \leq 1.5$ (figure 4.6) as the separation on the outer shoulder is affected by the front wheel jetting vortex and wheelhouse outflow. Vortex L protrudes in the spanwise direction for $ws/d \leq 1.5$, becomes disrupted by the front wheel outboard jetting vortex at $ws/d = 1.5$ and contributes to the reduction of rear wheel drag. With Vortex L projecting further outboard, the $L_1$ vortex that has been identified using higher fidelity simulations becomes more evident [16]. This comes as a result of the increased resolution at the wheel-ground contact compared to other RANS simulations [11, 13, 18]. Vortex C is only a small formation at the rear wheelhouse while vortex S shows significant interaction with the outer shoulder of the rear wheel, preventing outflow from the rear part of the wheelhouse. The new C vortex moves inboard and across the top of the wheel, merging with vortex A for $ws/d \leq 1.5$ and suppressing the formation of vortex B. This forces vortex E to merge downstream with the inboard jetting vortex R which results in the reduction of rear wheel drag. However, the change in outflow from vortex E sees an increase in rear wheelhouse drag.

(a) $ws/d = 0.5$      (b) $ws/d = 1.0$      (c) $ws/d = 1.5$
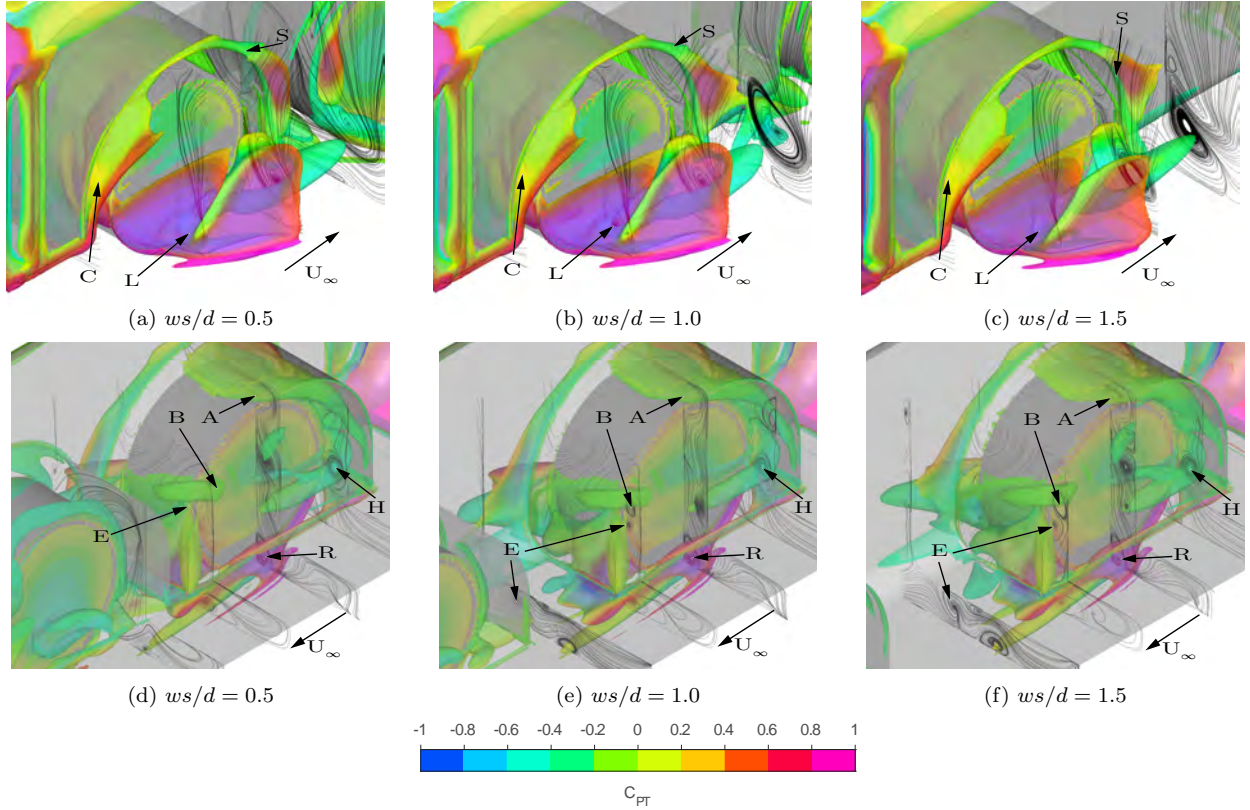
(d) $ws/d = 0.5$      (e) $ws/d = 1.0$      (f) $ws/d = 1.5$
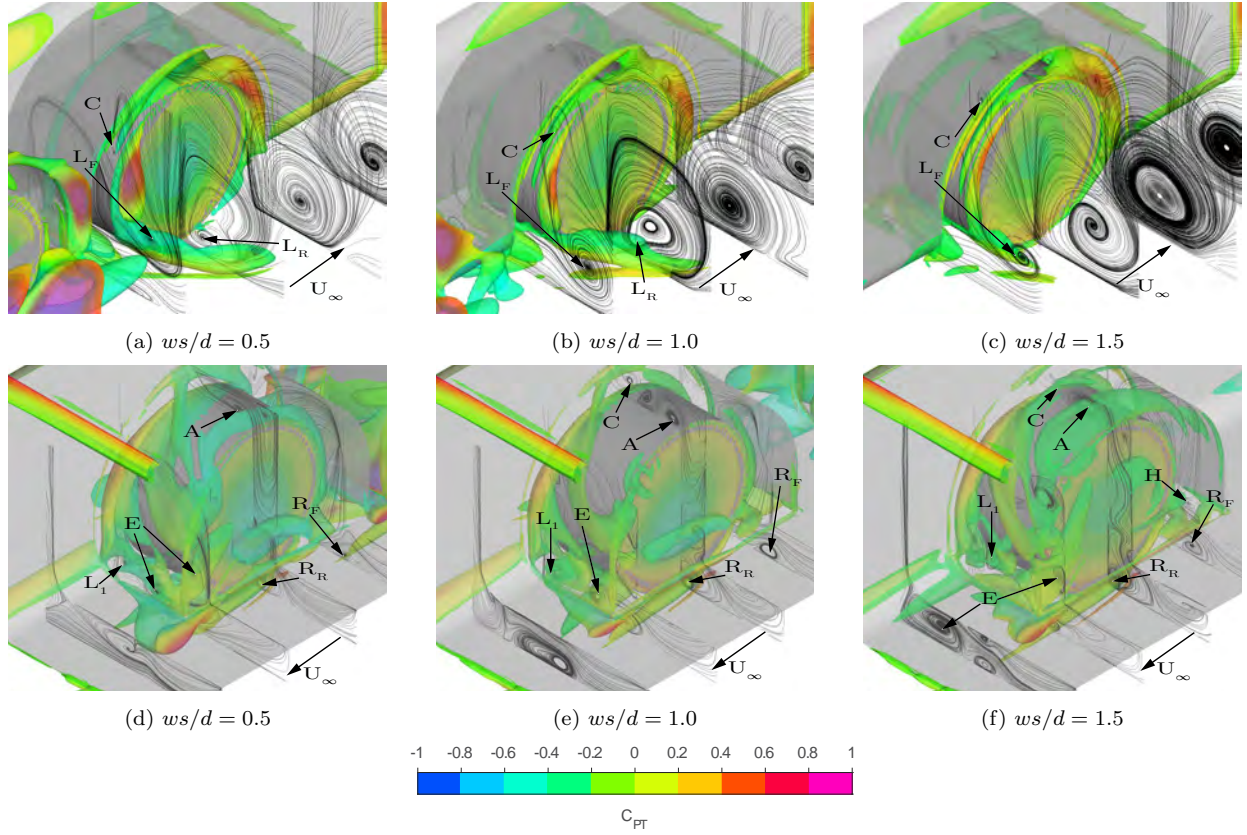
Figure 4.6: Vortex cores around the rear wheel with varying wheel spacing with overhang $le/d = 1$, plotted with $Q = 3.2 \times 10^5 \ s^{-2}$, $\alpha = 0.45$

### 4.1.2.1    Rear Wheelhouse Inflow

Flow into the rear wheelhouse varies based on the proximity of the rear wheel to the front. Longer wheel spacing $ws/d > 1.5$ allows for the upstream L and E vortices from the front wheel to expand and begin to dissipate before reaching the rear wheel. A wheel spacing of $ws/d \leq 1.5$ impedes the formation of some typical, rear-wheel vortices. This impediment of the L vortex significantly changes the rear wheelhouse flowfield from $ws/d < 1.5$, resulting in an increase in rear wheelhouse and total drag. The most obvious of these is the jet-like structure formed from the front wheel inboard jetting vortex merging with vortex E and protruding in the spanwise direction at the rear wheel contact point, influencing the formation of vortex L from the rear wheel (figure 4.7).

Further up the body away from the ground plane, the front wheel wake creates an outflow at the front of the rear wheelhouse and is linked to the reduction in size of the H vortex (figures 4.7g-4.7i). This outflow creates flow separations on the rear wheel shoulder, changing the direction and magnitude of the rear outboard jetting vortex. It is most prominent in the smallest spacing case, suggesting that the outflow from the front of the rear wheelhouse is crucial to reducing drag

28
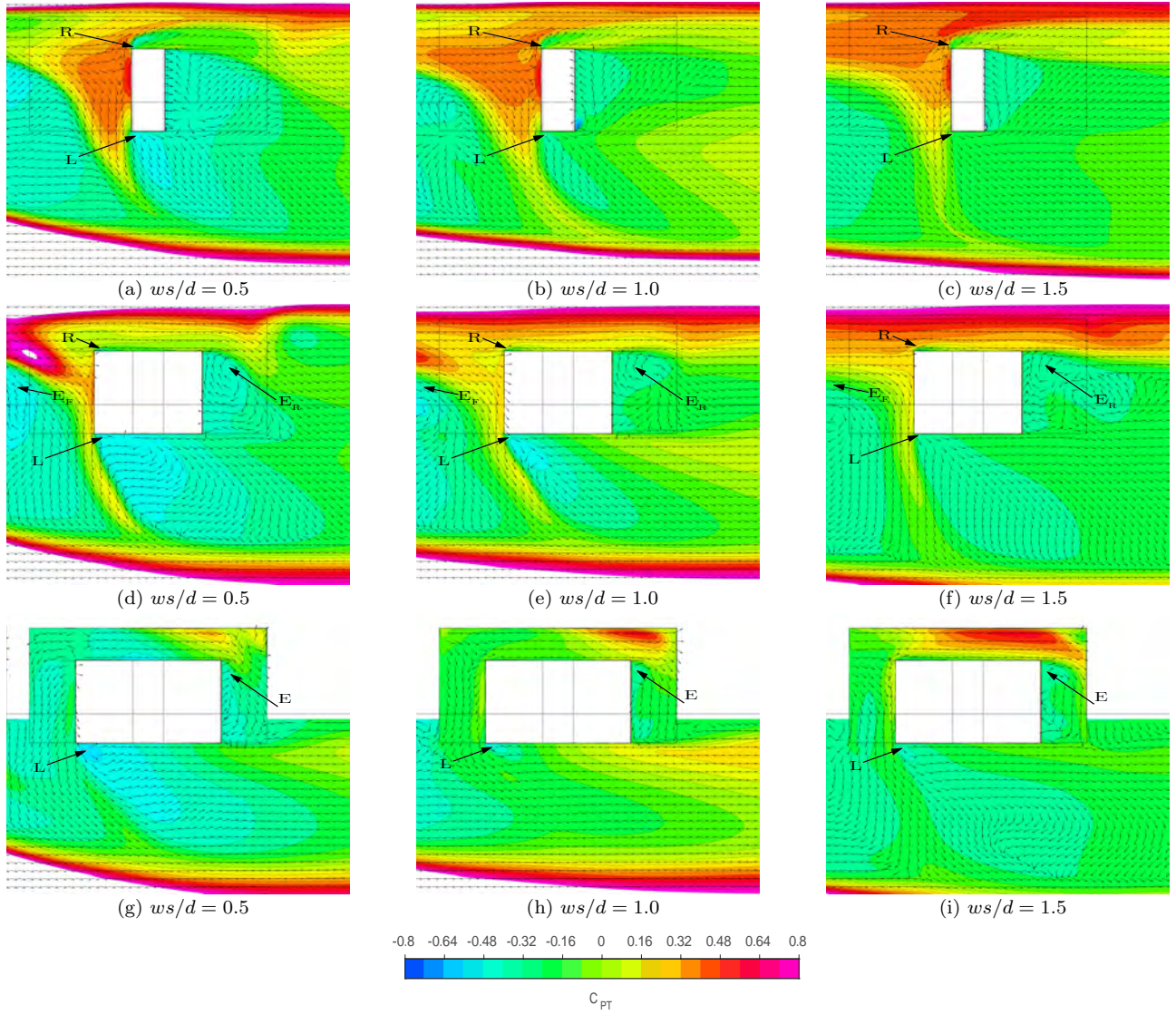
Figure 4.7: (a-c) Flow at the wheel-ground contact patch with varying wheel spacing with overhang $le/d = 1$; (d-f) Wheel flow at the midplane between the ground and underbody $z/d = 0.1$; (g-i) Wheelhouse outflow at the underbody plane $z/d = 0.22$

at the rear wheel. The same flow field however has a significant increase in rear wheelhouse drag more than the reduction of rear wheel drag. Furthermore, drag across the side face of the body is highest for $ws/d = 0.5$ and gradually reduces as wheel spacing increases and the formation of vortex L at the rear wheel is less affected by the upstream flow.

Flow through the inner wheelhouse presents variations in the vortices and flow rotations, namely the rotation near the centre of the wheel (figure 4.8a-4.8c) which appears much stronger than it does with the front wheelhouse. Vortex B reduces in strength as wheel spacing increases. Formation of vortex H in the rear wheelhouse is influenced by the presence of the stronger E vortex from the front wheelhouse for $ws/d < 1.5$ (figure 4.8d-4.8f) as a result of the lower total pressure and
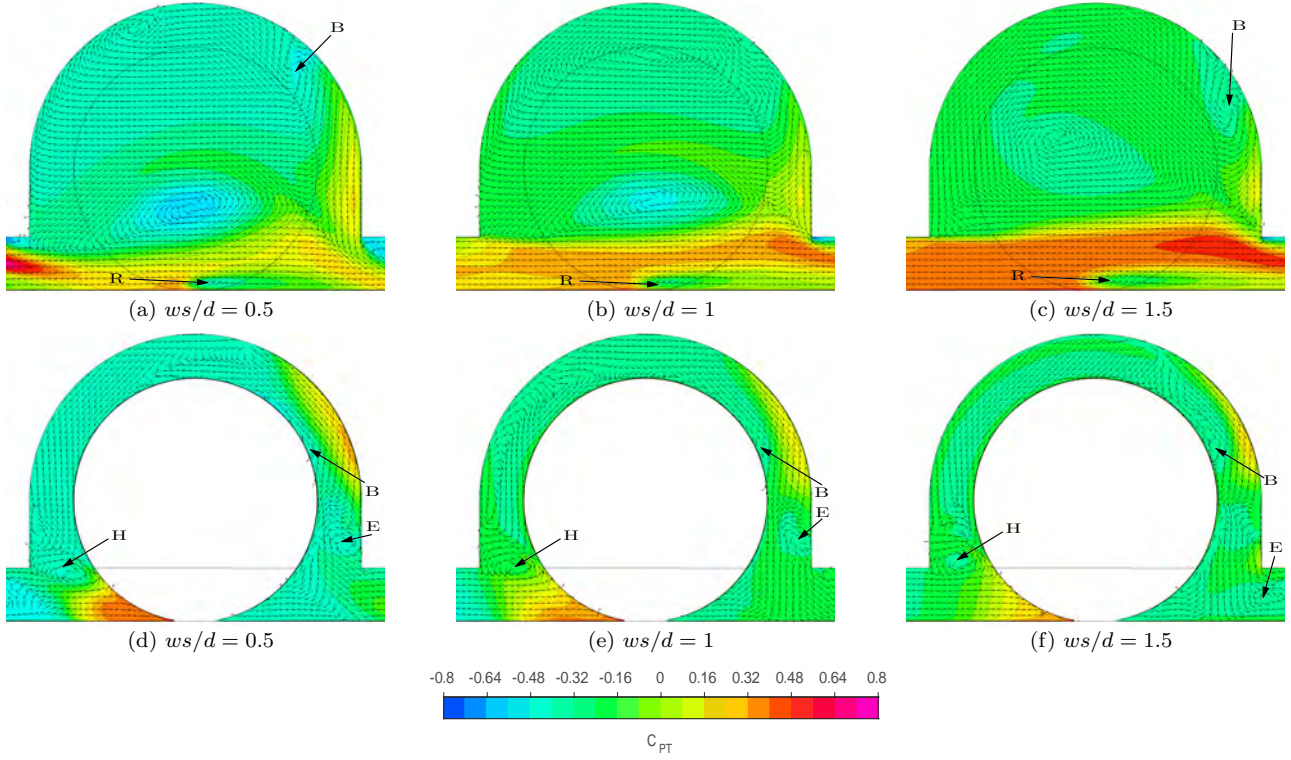
Figure 4.8: Flow in the front wheelhouse with varying wheel spacing with overhang $le/d = 1$; (a-c) Inner wheelhouse $y/d = 0.68$; (d-f) wheel midplane $y/d = 1$

flow direction through the inner wheelhouse. The flow within the front of the rear wheelhouse is projected away from the body in the spanwise direction and drawn towards the wake of the front outboard jetting vortex; preventing the underbody flow from rolling up into the wheelhouse and forming the H vortex. This has additional effects downstream as vortex H can no longer aid the formation of vortex E on the inner shoulder of the rear wheel and reducing rear wheelhouse outflow into the underbody.

There is a strong interaction between the outboard wake of the front wheel and the formation of the rear wheel L vortex. Wheel spacing $ws/d < 1.5$ sees the vortex L of the rear wheel gain strength from the rotation generated from the front wheel as they are co-rotating and positioned closer to the rear wheel than seen in other cases (figures 4.9d, 4.9e). As the spacing reaches $ws/d = 1.5$ the vortex L is suppressed (figure 4.9f). The vortex returns for spacing $ws/d > 2$ with reduced rotation and less effect on the rear wheelhouse flowfield. The front wheel inner jetting vortex can be seen towards the front of the rear wheelhouse for wheel spacing $ws/d \leq 1.5$ however is dissipated and does not affect the formation of the R vortex at the real wheel.
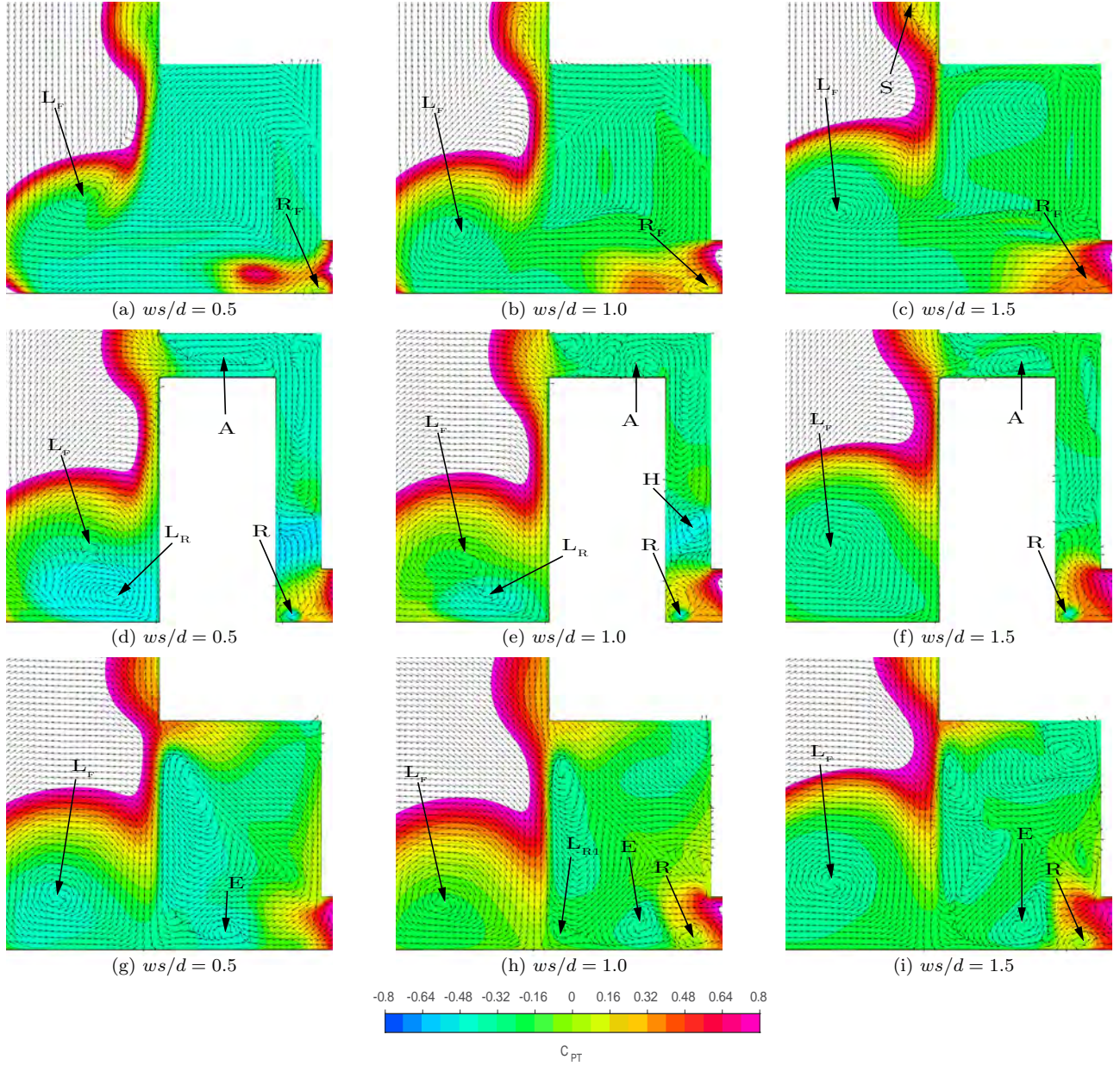
Figure 4.9: Total pressure across streamwise planes through the rear wheelhouse with varying wheel spacing with overhang $le/d = 1$; (a-c) $x_{rw}/d = -0.5$; (d-f) $x_{rw}/d = 0$; (g-i) $x_{rw}/d = 0.5$

#### 4.1.2.2 Rear Wheelhouse Outflow

The E vortex is still present in the inner rear wheelhouse despite the change in the H vortex and remains prominent as it moves into the underbody with the exception of $ws/d = 0.5$, where the formation is prevented due to the large wake from the front wheel (figure 4.10). It begins to dissipate closer to the wheelhouse for $ws/d = 1$ and maintains strength downstream for $ws/d \geq 1.5$ before dissipating into the wake behind the body due to another vortex shed from the lower inner face of the wheelhouse. This change in vortex E is also responsible for increased drag across the rear

face of the body, with rear face drag reducing as vortices E and R no longer merge for $ws/d \geq 1.5$.



(a) $ws/d = 0.5$        (b) $ws/d = 1.0$        (c) $ws/d = 1.5$

-0.8  -0.64  -0.48  -0.32  -0.16  0  0.16  0.32  0.48  0.64  0.8

$C_{PT}$
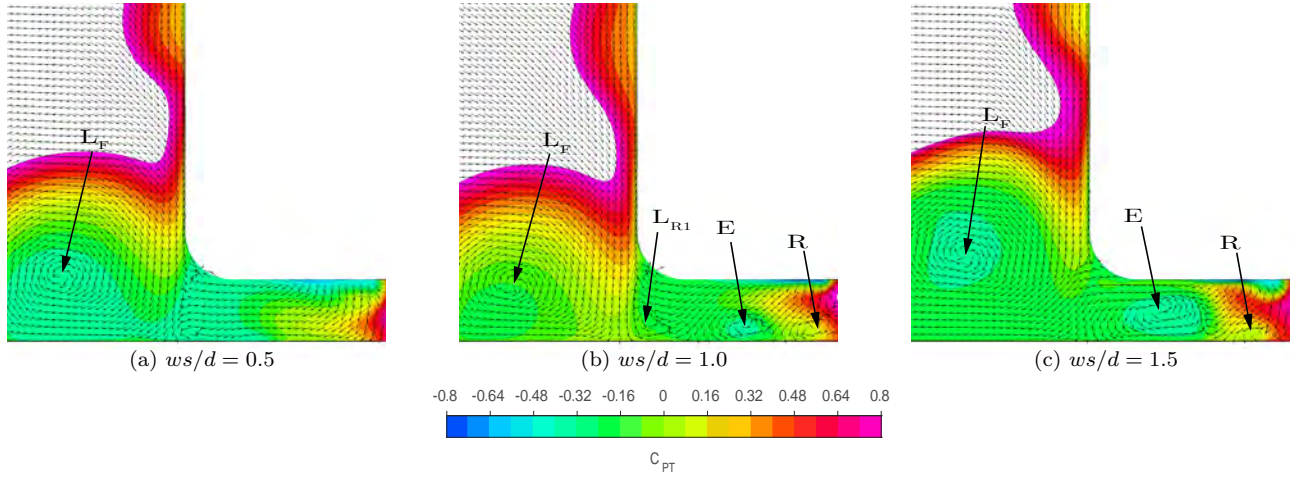
Figure 4.10: Total pressure across streamwise planes with varying wheel spacing with overhang $le/d = 1$ at $x_{fw}/d = 0.69$

#### 4.1.2.3   Rear Wheelhouse Pressure

Surface pressure through the rear wheelhouse is highly dependant on the proximity of the front wheel. Larger negative pressure regions on the forward face cause the drag increase of the wheelhouse for $ws/d = 0.5$. The pressure drop is a result of the increased strength of vortex A (figure 4.9d). This pressure is continued to the upper wheelhouse, resulting in a suction force across the surface, significantly reducing lift. The same pressure field acts on the wheel leading to a minor lift increase which is a result of the E vortex from the front wheelhouse splitting and being drawn into the upper rear wheelhouse, influencing the strength of vortex A and affecting the formation of vortex H. An interaction between the front inboard jetting vortex and the inner rear wheel shoulder creates a new rotation between the inner wheelhouse and wheel. This rotation further reduces inner wheelhouse pressures (figures 4.11a and 4.11b), making a large contribution to the change in lift and drag for the rear wheel and wheelhouse. Pressure recovers for wheel spacings $ws/d > 2$ with no further changes occurring in lift force. This allows for the pressure gradient to return across the rear wheel which results in a drag increase from $ws/d = 2$ as the wheel spacing increases.

|  |  |  |
|---|---|---|
| (a) $ws/d = 0.5$ | (b) $ws/d = 1.0$ | (c) $ws/d = 1.5$ |
| (d) $ws/d = 0.5$ | (e) $ws/d = 1.0$ | (f) $ws/d = 1.5$ |

-0.5  -0.4  -0.3  -0.2  -0.1   0   0.1   0.2   0.3   0.4   0.5

$C_p$
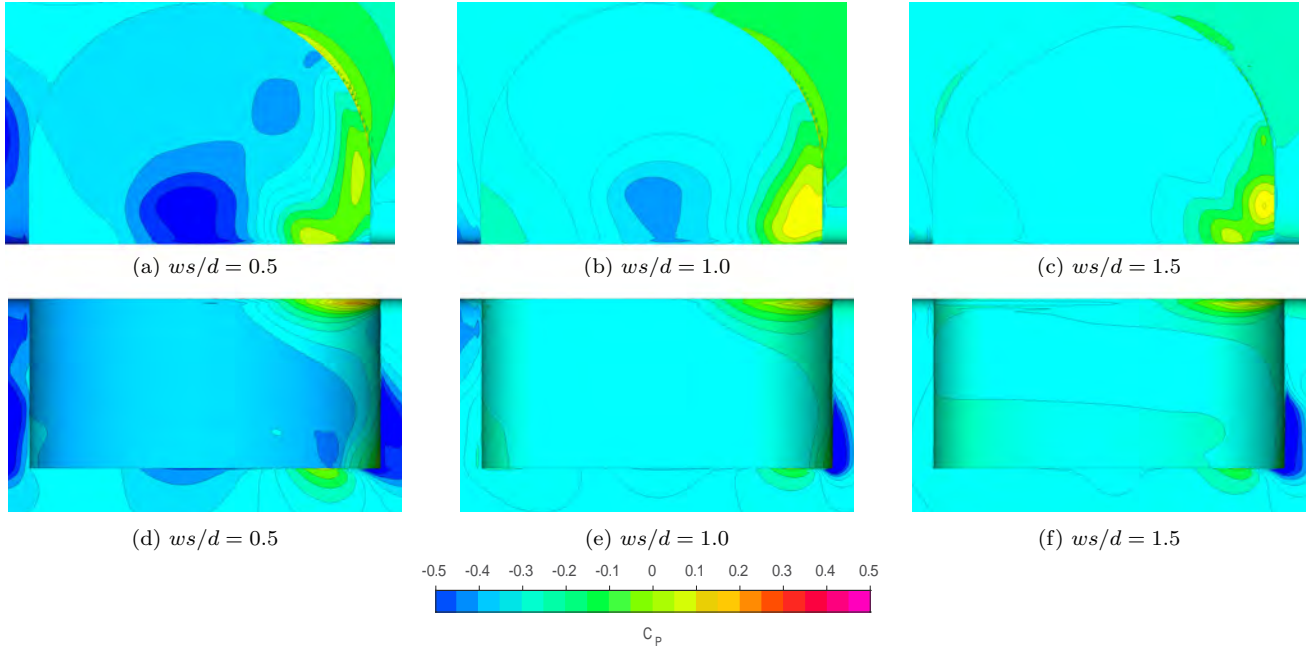
Figure 4.11: $C_p$ Rear wheelhouse with varying wheel spacing with overhang $le/d = 1$; (a-c) side view; (d-f) bottom view

## 4.2 Isolating the Effects of Varying Overhang

### 4.2.1 Front Overhang Variations

In this section, front overhang $le$ was varied whilst $te$ was held constant to investigate the effect of changing vehicle overhang. Four overhang variations, $le/d$, were simulated from 0.5 to 2 in increments of 0.5. Drag force over the front wheel experienced a 7% drag reduction with the smallest overhang while lift was increased 60% (figure 4.12a). Front wheelhouse drag remained as a minor contributor to overall drag with small changes. Lift was significantly influenced by the shorter overhang exceeding almost 5 times the lift of the longest overhang case (figure 4.12b). Minor lift and drag variations occurred in the rear and were not dependant on the front overhang length.

The interaction between the front face and front wheelhouse can be identified by the change in vortex structures generated by the wheelhouse. The C vortex generated by the forward arch of the wheelhouse is much more prominent than in the longer overhang cases (figure 4.13a-4.13c), in addition to the outboard jetting vortex L being disturbed by the large separation from the upper wheel edge. This separation spans outwards creating a larger wake than what the formed outboard jetting vortex would (figure 4.14). The more defined L vortex maintains rotation further

(a) $C_D$         (b) $C_L$
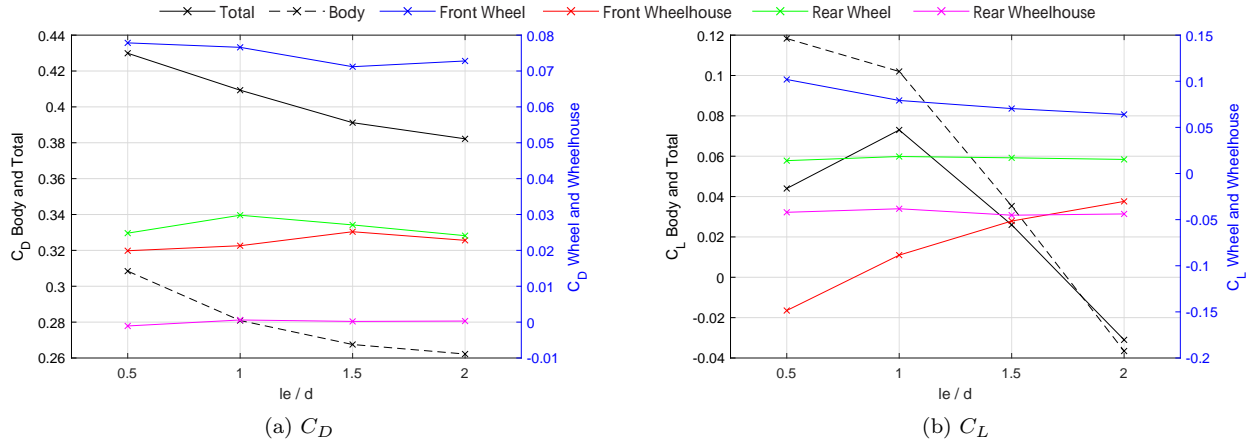
Figure 4.12: Force coefficients for varying front overhang with wheel spacing $ws/d = 3.0$



(a) $le/d = 0.5$     (b) $le/d = 1.0$     (c) $le/d = 1.5$

(d) $le/d = 0.5$     (e) $le/d = 1.0$     (f) $le/d = 1.5$
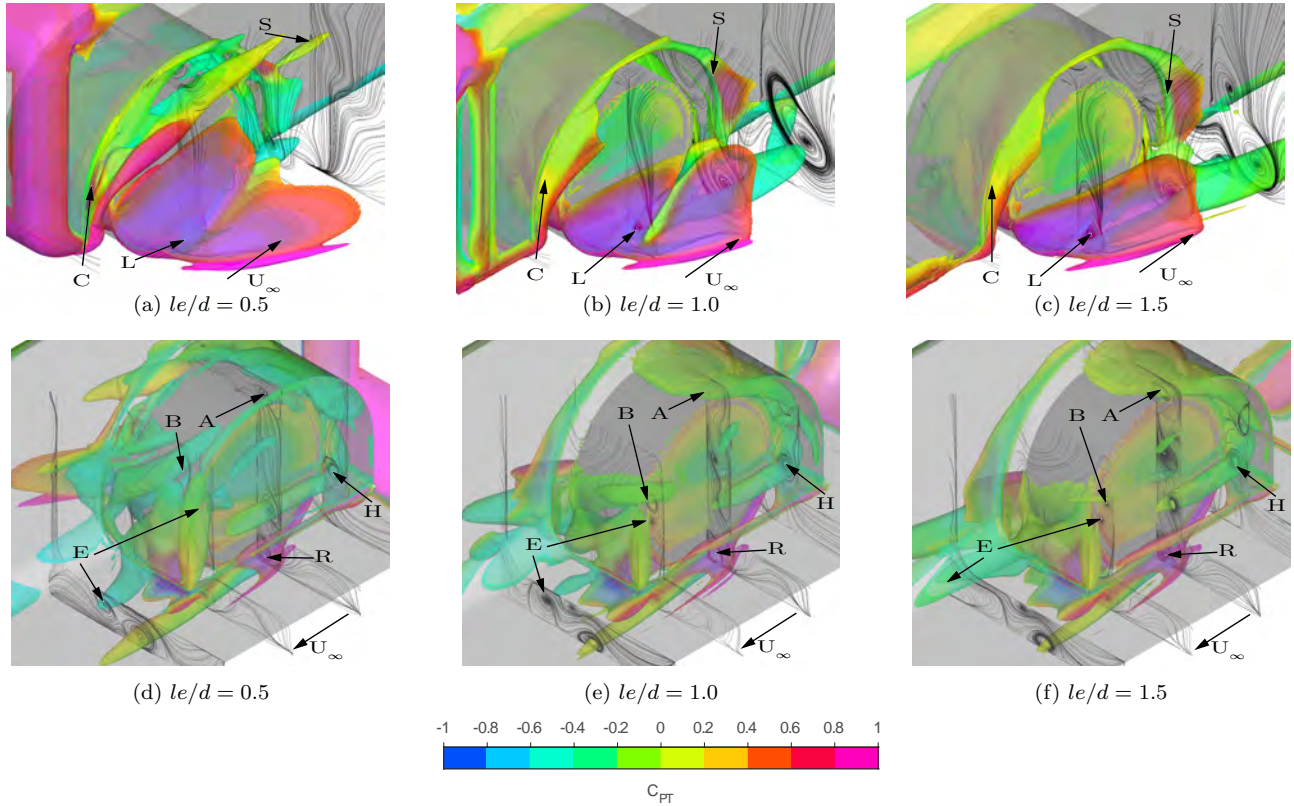
Figure 4.13: Vortex cores around the front wheel for varying front overhang with wheel spacing $ws/d = 3.0$ plotted with $Q = 3.2 \times 10^5 \ s^{-2}$, $\alpha = 0.45$

downstream and remains closer to the wheel and ground for wheel spacing $ws/d \geq 1$.

Flow structures within the wheelhouse also experience some change. The H vortex is affected by the overhang length, with the shorter overhang exacerbating the strength of the rotation (figures 4.13d-4.13f), similar to the H vortex of the rear wheelhouse from section 4.1.2.1. Position and size of vortex E is dictated by vortex H, positioned towards the centre of the wheel in the wheelhouse for the shortest overhang case as opposed to just above the ground plane. An additional vortex
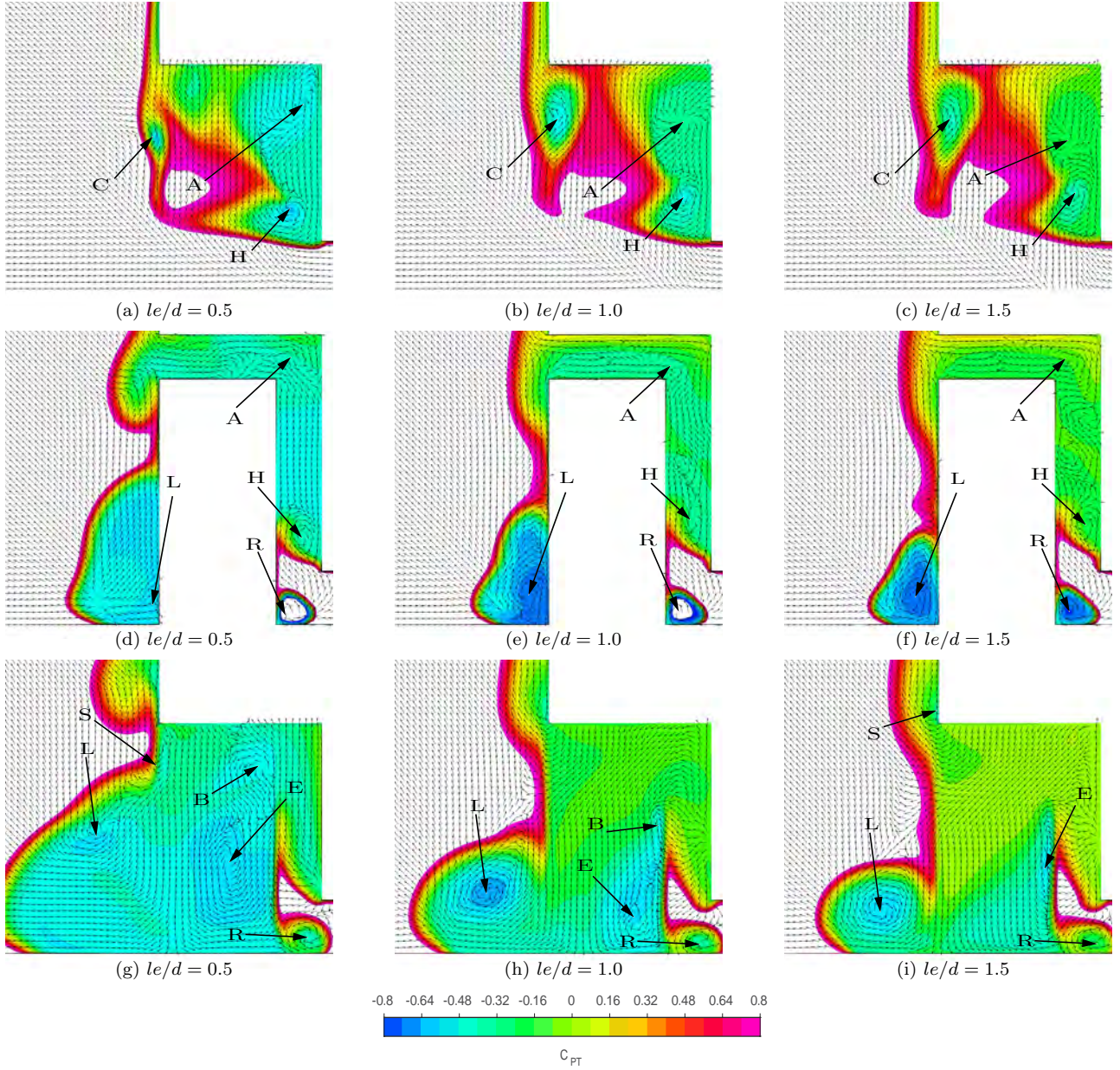
Figure 4.14: Flow features within the front wheelhouse for varying front overhang with wheel spacing $ws/d = 3.0$; (a-c) $x_{fw}/d = $ -0.5; (d-f) $x_{fw}/d = 0$; (g-i) $x_{fw}/d = 0.5$

is present at the top inside corner of the wheelhouse (figure 4.14a) which has not appeared in the previous cases on this plane and likely to be an extension of vortex A. Previous authors noted that vortices A and B are dependent on the wheelhouse ratio and it appears to also be related to the front overhang [13].

The wheel wake for $ws/d = 0.5$ is larger than the longer overhang cases (figure 4.14g). Flow within the wake has rotation further away from the ground than vortex L seen for $ws/d > 1$ (figures 4.14h, 4.14i). Vortex C interacts with the upper wheel edge, drawing air upwards and creating a lower

pressure region where vortex L would form and is formed downstream closer to vortex S (figure 4.14g). The lower total pressure draws vortex E from the underbody further downstream and creates a new rotation $1.5d$ behind the plane tangent to the back of the front wheel.
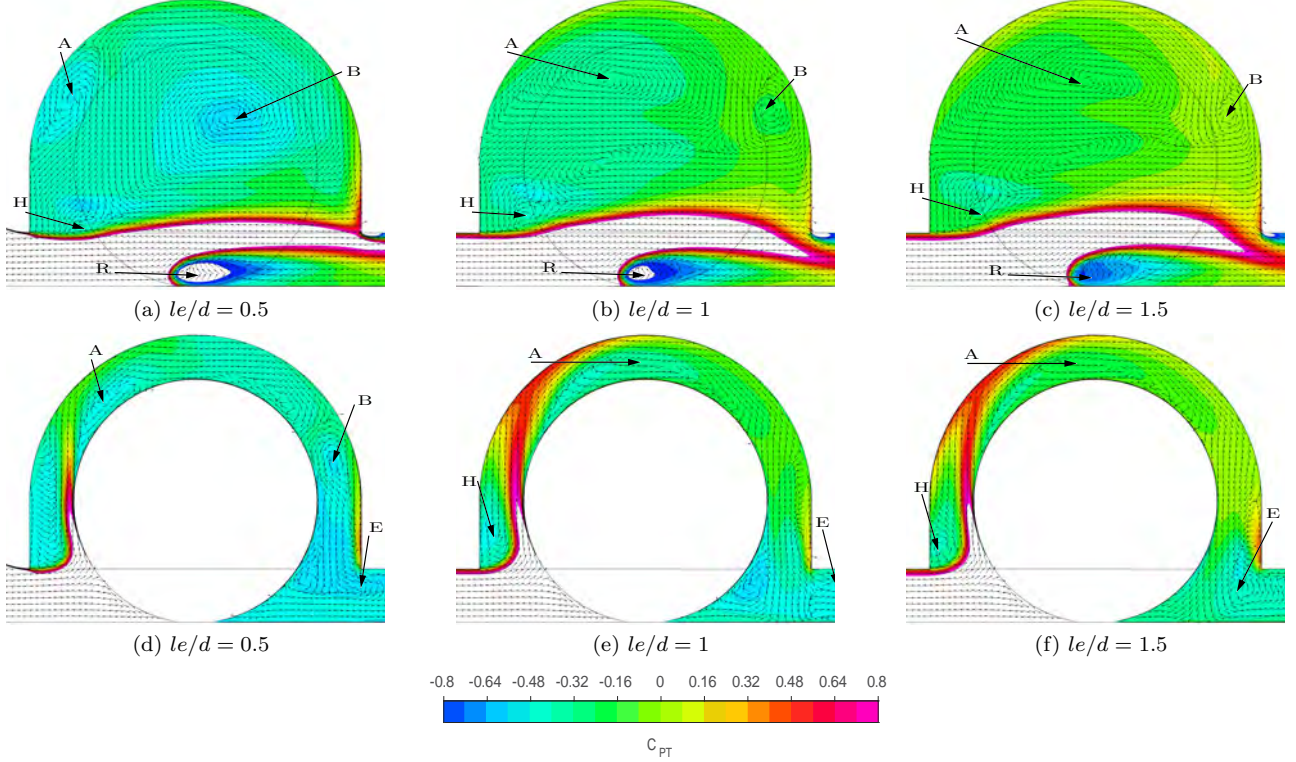


Figure 4.15: Flow in the front wheelhouse for varying front overhang with wheel spacing $ws/d = 3.0$; (a-c) Inner wheelhouse $y/d = 0.68$; (d-f) wheel midplane $y/d = 1$

The front wheel wake has extended rearward with the rotation in the flow being extended further in the underbody. Both A and B vortex cores are prominent in $ws/d = 0.5$, although a third vortex is also present and could be an extension or splitting of either A or B (figure 4.15d). The additional strength in the H vortex is caused by the yawed inflow into the wheelhouse and moves further downstream along the inner face of the wheel where it is exacerbated and enhances the strength of the E vortex (figures 4.15a-4.15c). Direction of the flow through the upper wheelhouse is also moving against the freestream direction as a result of the strengthened H vortex. The longer overhang cases show no unique features for $ws/d > 1$.

Flow from the vortices L and R at the ground are more notable for $ws/d = 0.5$. The outboard wake spans out much wider than $ws/d \geq 1$, with backflow continuing as far as the rear wheelhouse and forming a much larger wake from the front wheel (figures 4.16d-4.16f). Vectors at the front wheel are in agreement with previous studies as the shorter overhang increases the yaw of the oncoming flow [6, 13, 14]. The front face of the body is the most sensitive to the change in overhang with
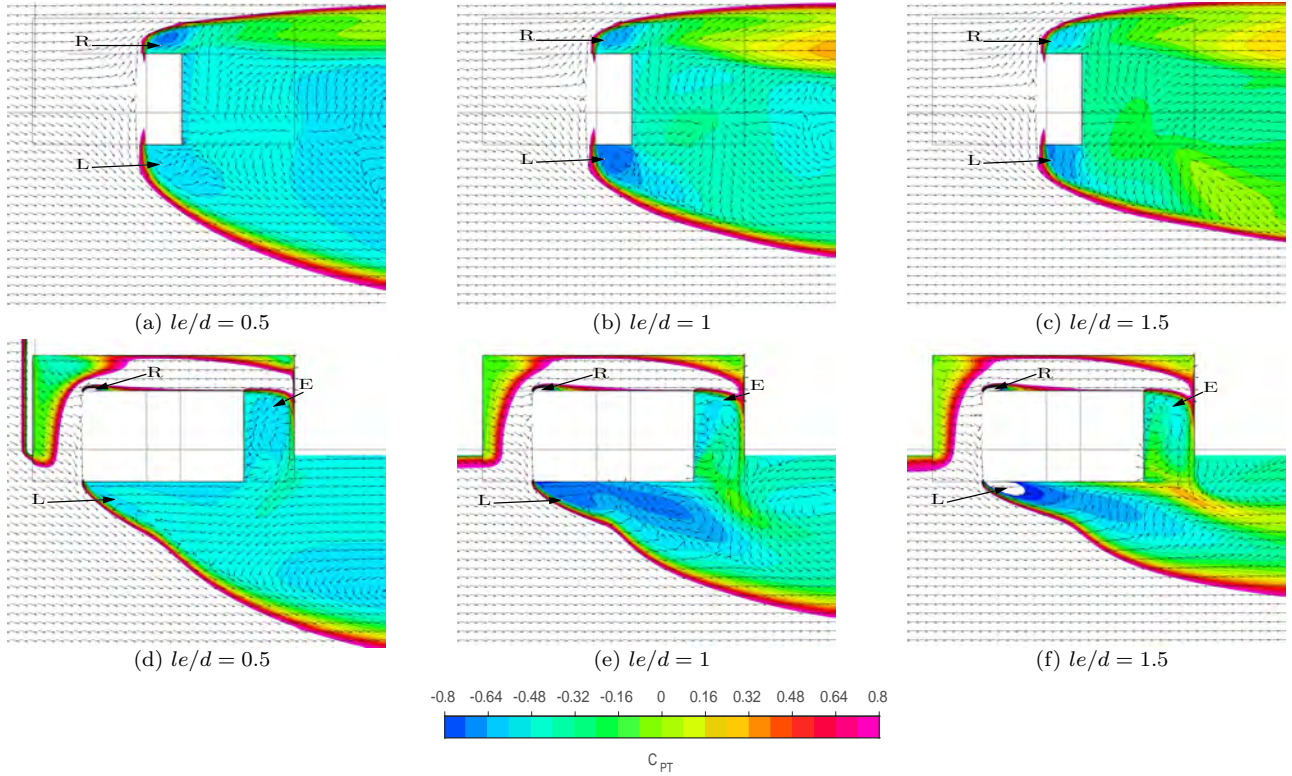
Figure 4.16: (a-c) Flow at the wheel-ground contact patch for varying front overhang with wheel spacing $ws/d = 3.0$; (d-f) Wheelhouse outflow in-line with the underbody $z/d = 0.22$

the shorter overhang responsible for the significant changes in the body forces observed. This is a result of the higher static pressure on the lower radius of the front face, caused by the increase in yawed flow into the front wheelhouse (figure 4.16d).

The outboard rotation from $ws/d = 0.5$ is still prominent further from the ground plane, maintaining a stronger backflow along the side of the body and reducing outflow from the rear of the wheelhouse (figure 4.16). Flow into the rear wheelhouse shows some minor obstruction however is not significant enough to create noticeable effects. The larger wheel wake from the front wheel detaches the boundary layer on the side of the body, resulting in a significant increase in drag.

### 4.2.2 Rear Overhang Variations

Variation in rear overhang length produced the least amount of force change of all the configurations tested in this study. No significant change is observed in wheel or wheelhouse drag for the varying length of the rear overhang and total drag varying no more than 0.8%. Variations in total lift were greater for $ws/d < 1.5$ (figure 4.12) at 30% however this was attributed to the increased surface area of the top face and underbody. Pressure along the underbody forward of the rear wheel is

identical for all cases and returns to static as it reaches the rear wheelhouse. Flow structures around the wheels and body are consistent for all rear overhang cases tested and have not shown any unique flow features.



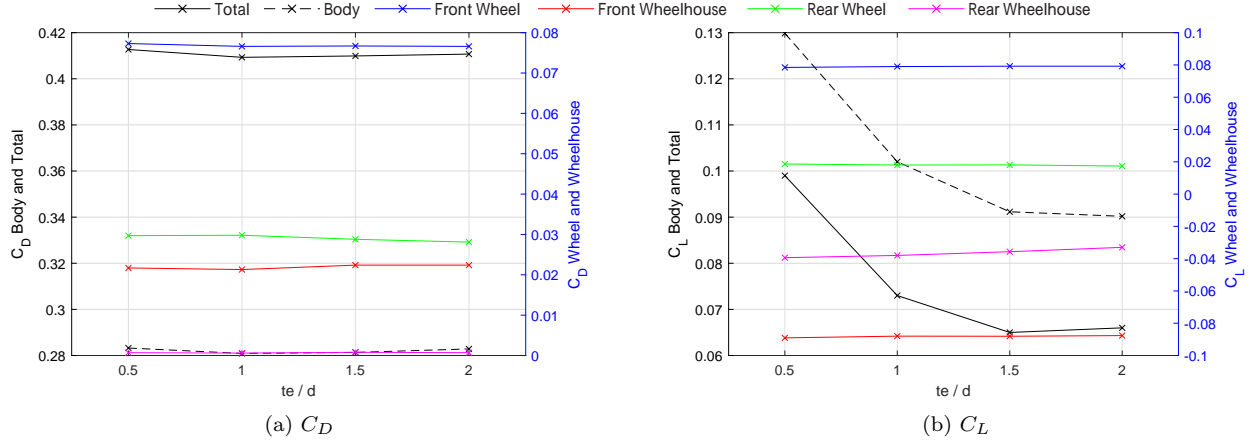Figure 4.17: Force coefficients for varying rear overhang

## 4.3    Influence of Overhang on Wheel Spacing

A significant variation in front wheelhouse outflow was observed in section 4.2.1 between the varying overhang cases. Vortices L and E have been identified as having potential to impact the flowfield downstream at the rear wheel and required further investigation into how their effects would transpire with varying wheel spacing. Vortex L was observed to significantly change for the varying overhang lengths. Shorter lengths produced a much larger wake region that further affected vortex E which was already significantly impacted by the varying rear wheel proximity. This influence had significant effects on the total forces for each overhang case (figure 4.18). It is expected that significant variations in the L and E vortices will be observed as wheel spacing is varied. As such, the initial study from section 4.1 has been repeated with front overhangs $le/d = 0.5$ and 1.5 as no significant changes were observed between $le/d = 1.5$ and 2.

A clear relationship between the front overhang, wheel spacing and drag has presented itself where minimum drag is a function of the two geometric factors. Minimum drag occurs at different wheel spacings for each overhang case (figure 4.18a) with the shortest overhang producing considerably more drag than the other two cases. Lift trends produce contrasting results to drag where the lift minimum is achieved at the same wheel spacing for each case at $le/d = 2$. Interestingly, the shortest overhang produces lift forces similar to that of the longest overhang at the minimum wheel

(a) $C_D$          (b) $C_L$
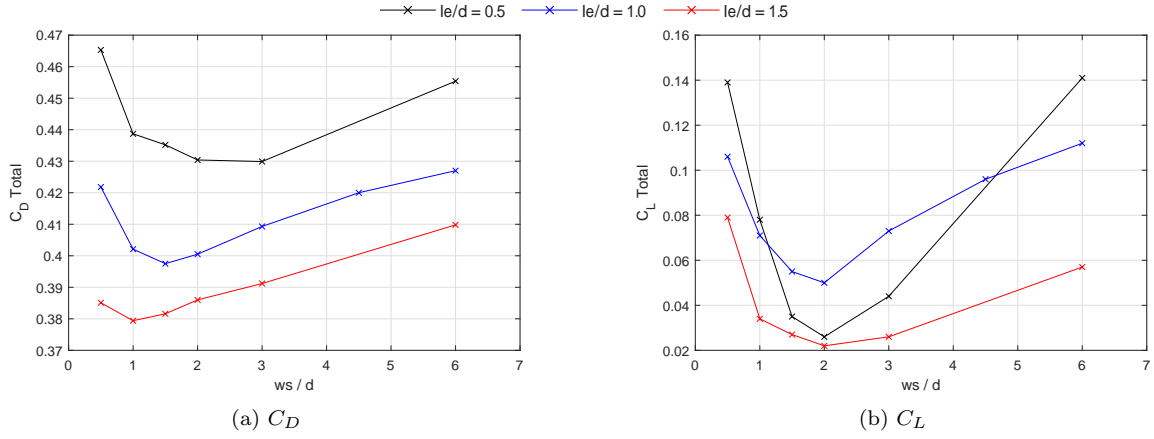
Figure 4.18: Total force coefficients for each overhang case

spacing but begins to increase significantly either side of the minimum. Further details on the flow structures responsible for these changes are discussed in the following sections.

### 4.3.1 Front Overhang $le/d = 0.5$

A significant drag force change occurs at $ws/d = 3$ (figure 4.19) as rear wheelhouse drag continues to be influenced by the upstream flow with drag increasing drastically. The point of minimum total lift remains the same as the $le/d = 1$ geometry however the drag minimum occurs at $ws/d = 3$. Rear wheel drag reduces for $ws/d < 3$ however begins to increase as spacings reduces beyond $ws/d = 1$, which is unique to this test variation.



(a) $C_D$          (b) $C_L$
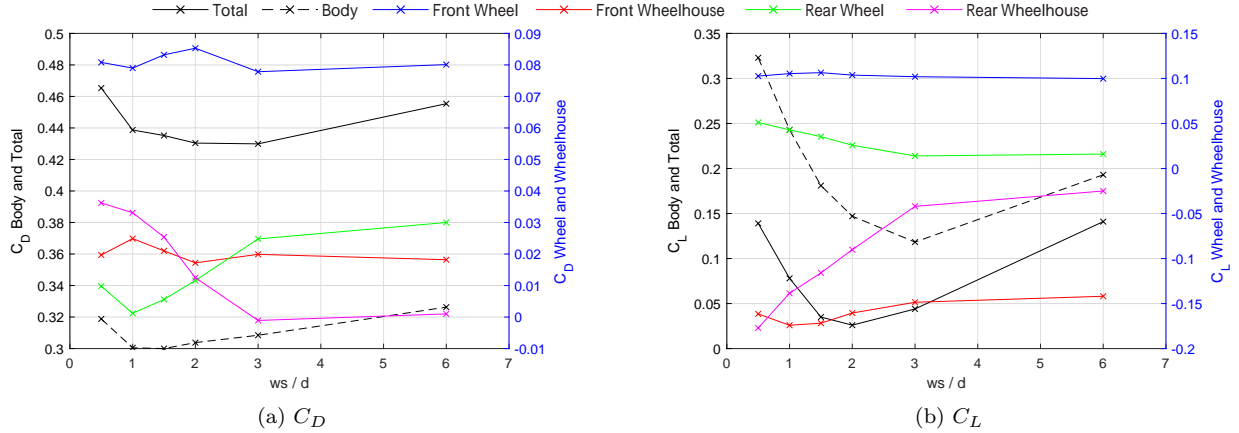
Figure 4.19: Force coefficients for front overhang $le/d = 0.5$

Flow entering the front wheelhouse is consistent for each wheel spacing however as the rear wheel is positioned closer to the front wheel, total pressure exiting the wheelhouse reduces and the E vortex becomes larger. As it continues downstream, it maintains strength in the underbody before

Figure 4.20: Vortex cores around the front wheel for varying wheel spacing with front overhang $le/d = 0.5$, plotted with $Q = 3.2 \times 10^5 \ s^{-2}$, $\alpha = 0.45$

merging with the H vortex in the rear wheelhouse. Vortices A and B have no significant changes in outflow, their flow across the top of the wheel does have some small variation that is caused from the change in formation of the H vortex. Vortex C reduces in length as wheel spacing reduces and cannot continue to form downstream. Instead it expands into the front of the wheelhouse and contributes to the H vortex, and hinders outflow of the A and B vortices from the top of the wheelhouse (figure 4.20a).

Rear wheel flow structures vary significantly for $ws/d \geq 2$. Vortex L is projected away from the body from $ws/d = 2$ (figure 4.21) and is a consistent flow feature that occurs as rear wheelhouse drag increases (figure 4.19a). For wheel spacing $ws/d < 1.5$ the formation of vortex L is significantly affected by the presence of the wheel ahead and forms larger structures that are projected away from the body. Vortex B is drawn from the upper wheelhouse inwards and down towards the E vortex which continues to flow into the underbody, no longer outflowing from the upper rear quadrant of the wheelhouse. This is prevented by a more dominant separation from the rear outer shoulder of the wheel which in turn hinders the formation of vortex S at the rear wheelhouse (figure 4.21). As with the $le/d = 1$ case, outflow through vortex E significantly reduces drag on the rear
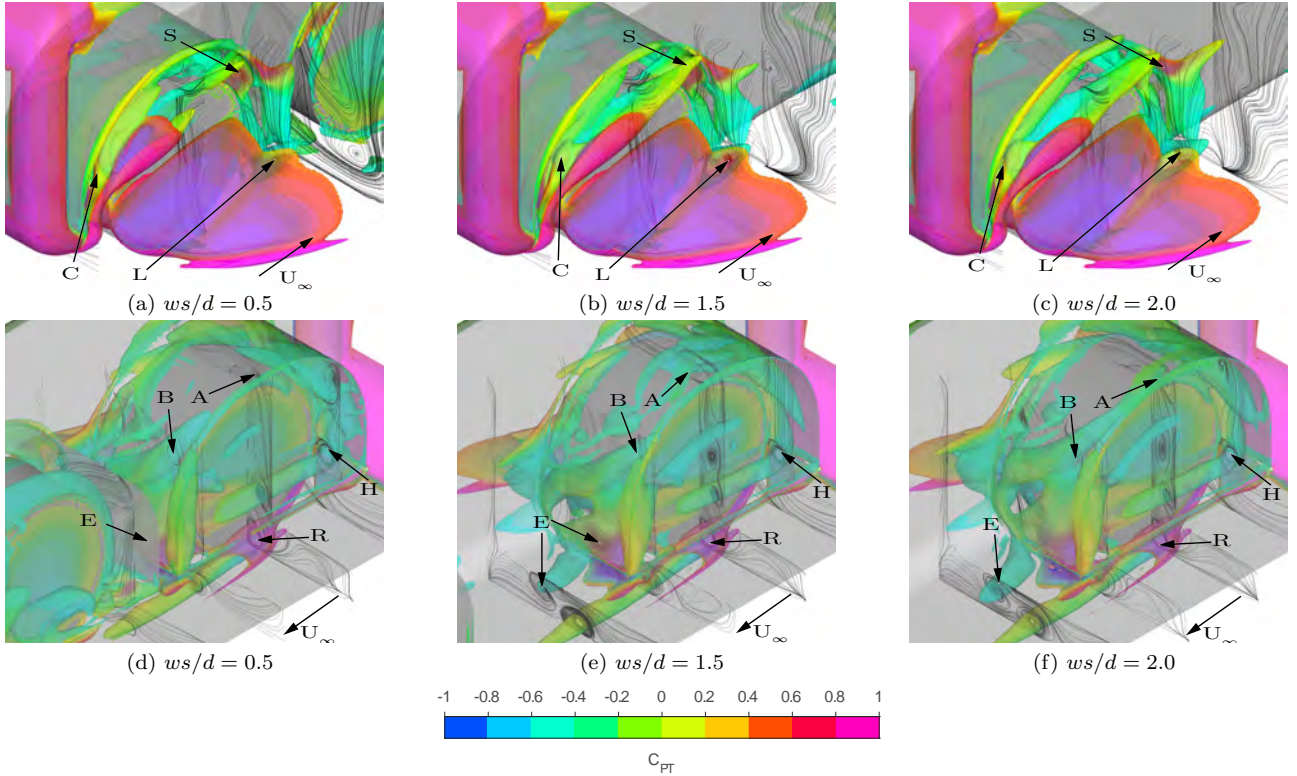
40
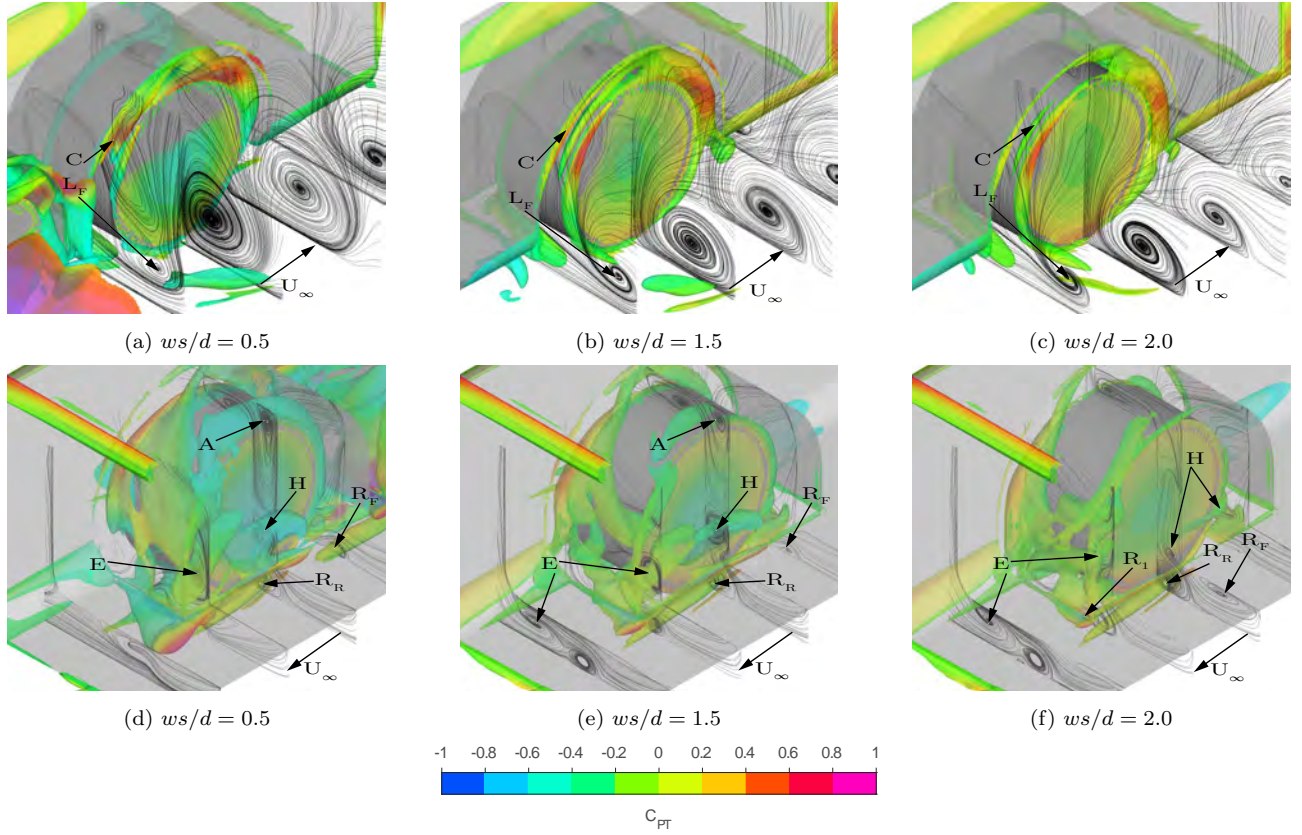
Figure 4.21: Vortex cores around the rear wheel for varying wheel spacing with front overhang $le/d = 0.5$, plotted with $Q = 3.2 \times 10^5 \ s^{-2}$, $\alpha = 0.45$

wheel.

Effects of the disrupted front outboard jetting vortex are seen downstream at the rear wheel where the larger wake has suppressed the formation of the rear outboard jetting vortex (figure 4.22). This was observed for the wheel spacings $ws/d < 1.5$ for the front overhang $le/d = 1$ case and are maintained for larger wheel spacings for the shorter front overhang geometry. Flow past the wheel is similar to the longer overhang cases. Vortex E is impacted by the shorter wheel spacing, changing outflow direction from the underbody to the spanwise direction. Interactions of greater intensity between vortices A and C above the wheel are formed. Outflow remains predominantly into the underbody through the E vortex and the H vortex extended further towards the rear of the wheelhouse.

Proximity of the rear wheel effects vortices A and B as vortex C is forced into the wheelhouse (figures 4.20, 4.21). The formation of vortex B towards the top rear quadrant of the wheel prevents vortex C continuing further downstream. Vortices B and E are prominent at the rear of the wheelhouse (figure 4.23a-4.23c) for each case along with the recirculation at the back of the wheel
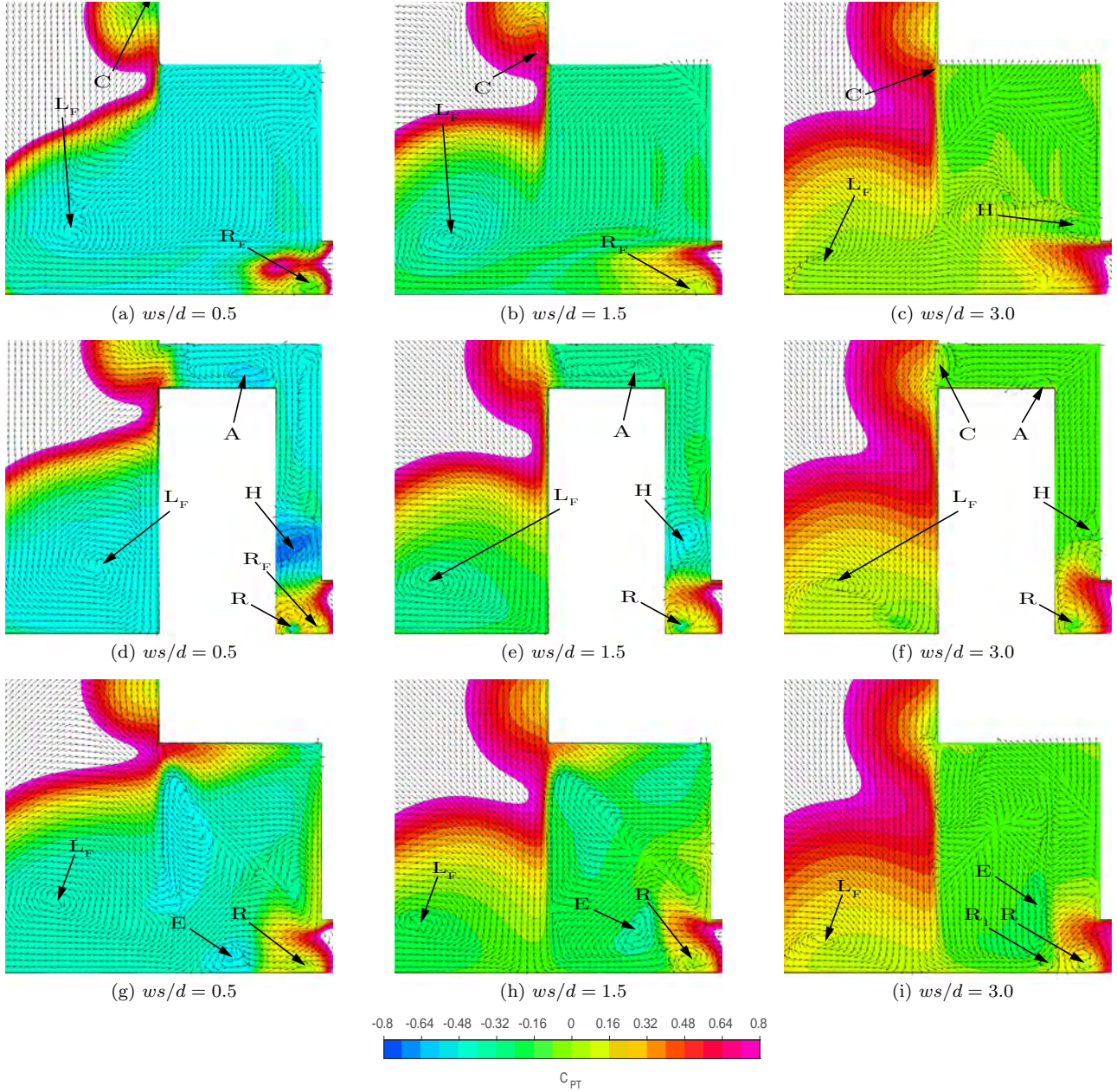
Figure 4.22: Flow features within the rear wheelhouse for varying wheel spacing with front overhang $le/d = 0.5$; (a-c) $x_{rw}/d = -0.5$; (d-f) $x_{rw}/d = 0$; (g-i) $x_{rw}/d = 0.5$

behind the contact patch. This rotation moves downstream as the rear wheel is placed closer to front, drawing the H vortex of the rear wheel towards the ground. In turn, total pressure increases at the rear wheel contact patch for $ws/d = 0.5$ (figure 4.23d), increasing drag with flow through the rear wheelhouse has a more downward trajectory. Rotation in the flow at the rear wheelhouse becomes more prominent after $ws/d > 1.5$ and the formation of the A, B and E vortices appear again (figure 4.23f).

Flow behind the rear wheel at the contact patch is more tangential to freestream flow for the
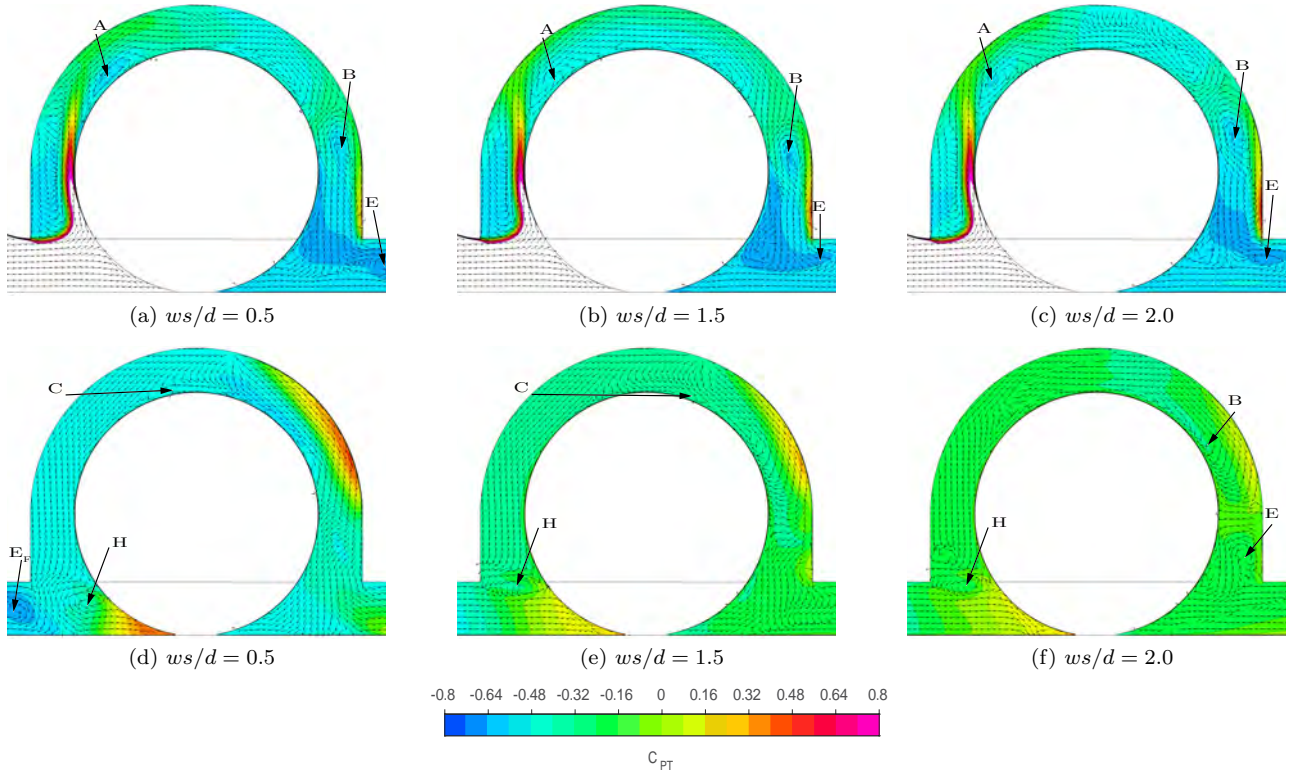
Figure 4.23: Flow across the wheel centreline for varying wheel spacing with front overhang $le/d = 0.5$; (a-c) Front wheel midplane $y/d = 1$; (d-f) Rear wheel midplane $y/d = 1$
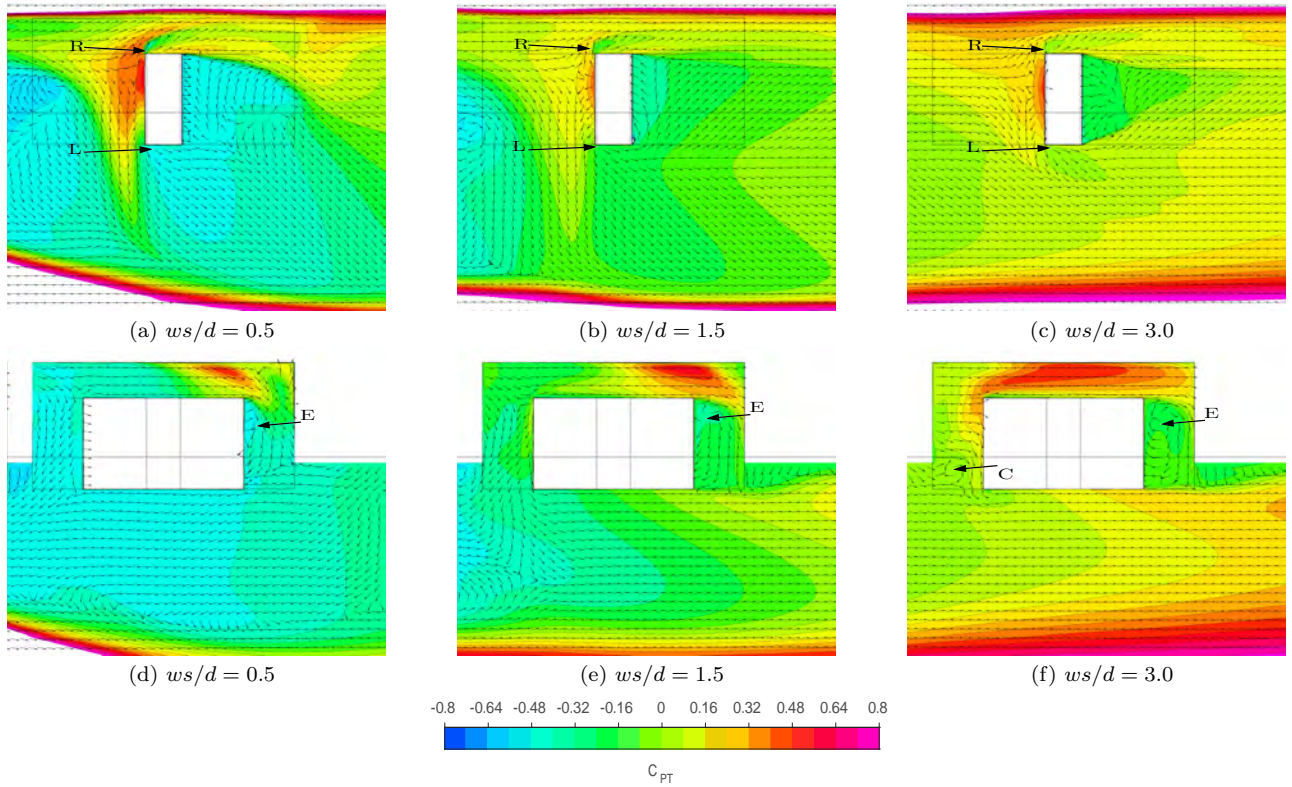


Figure 4.24: (a-c) Flow at the wheel-ground contact patch for varying wheel spacing with front overhang $le/d = 0.5$; (d-f) Wheelhouse outlflow inline with the underbody $z/d = 0.22$

43

$ws/d \leq 1.5$ (figures 4.24a, 4.24b). Total pressure buildup at the front of the rear wheel creates a larger recirculation behind the wheel forcing the flow in the spanwise direction. Further up in the wheelhouse, flow direction is against freestream for cases $ws/d < 1.5$ (figures 4.24d, 4.24e) drawing flow from the front of the rear wheelhouse into the wake of the front wheel. Flow from the rear of the wheelhouse is also drawn against freestream for $ws/d = 0.5$, resulting in increased drag for the rear wheel that was not observed for the front overhang $ws/d = 1$ cases.

### 4.3.2 Front Overhang $le/d = 1.5$

Front overhang of $ws/d = 1.5$ does not affect forces over the body as significantly as overhangs $le/d = 0.5$ or $le/d = 1.0$ (figure 4.25). Front wheel and wheelhouse lift is relatively consistent for each wheel spacing with minimal variation observed. Front wheel drag experiences a small increase whereas wheelhouse drag is decreased for $ws/d < 1.5$. Rear wheel drag has a steady reduction as wheel spacing decreases without the sudden drop in force as was seen with $le/d = 0.5$ and $le/d = 1.0$. Wheelhouse drag increases from $ws/d = 1.5$ though not as significantly as the shorter overhangs tested. Rear wheel and wheelhouse trends are similar to front overhang $le/d$ with minor variation in forces.



(a) $C_D$       (b) $C_L$
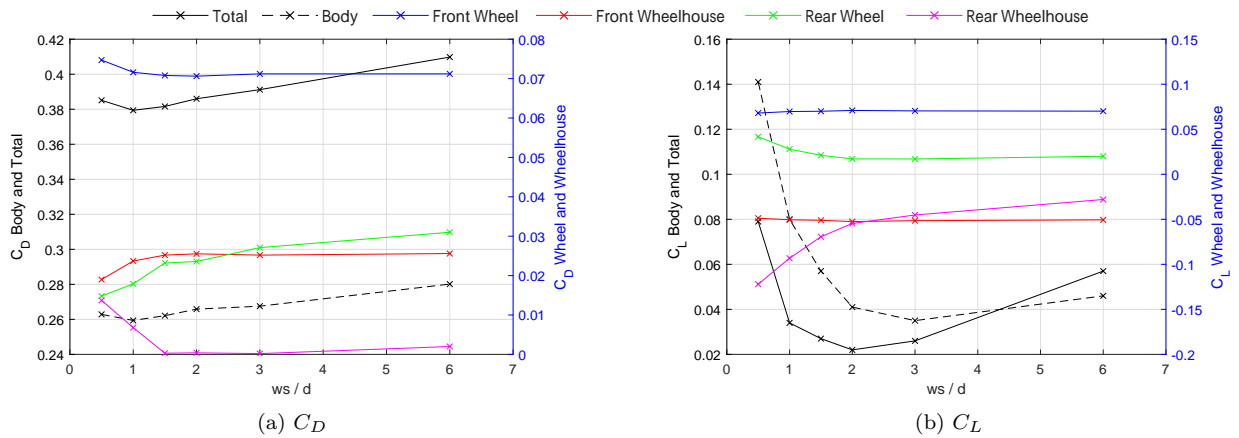
Figure 4.25: Force coefficient for $ws/d = 1.5$ Front Overhang

The longer overhang reduces the effect that the presence of the rear wheel has on vortex L generated by the front wheel (figures 4.26a-4.26c). Vortices A, B and C are also unaffected by the proximity of the rear wheel with only vortex S experiencing small changes to its structure due to the rear wheelhouse edge. Vortex L of the rear wheel is less disturbed than the shorter overhang geometries and does not project tangentially away from the body. Size does vary and is larger for the shorter wheel spaced cases (figures 4.27a-4.27c), which is consistent for all overhangs tested. Flow through
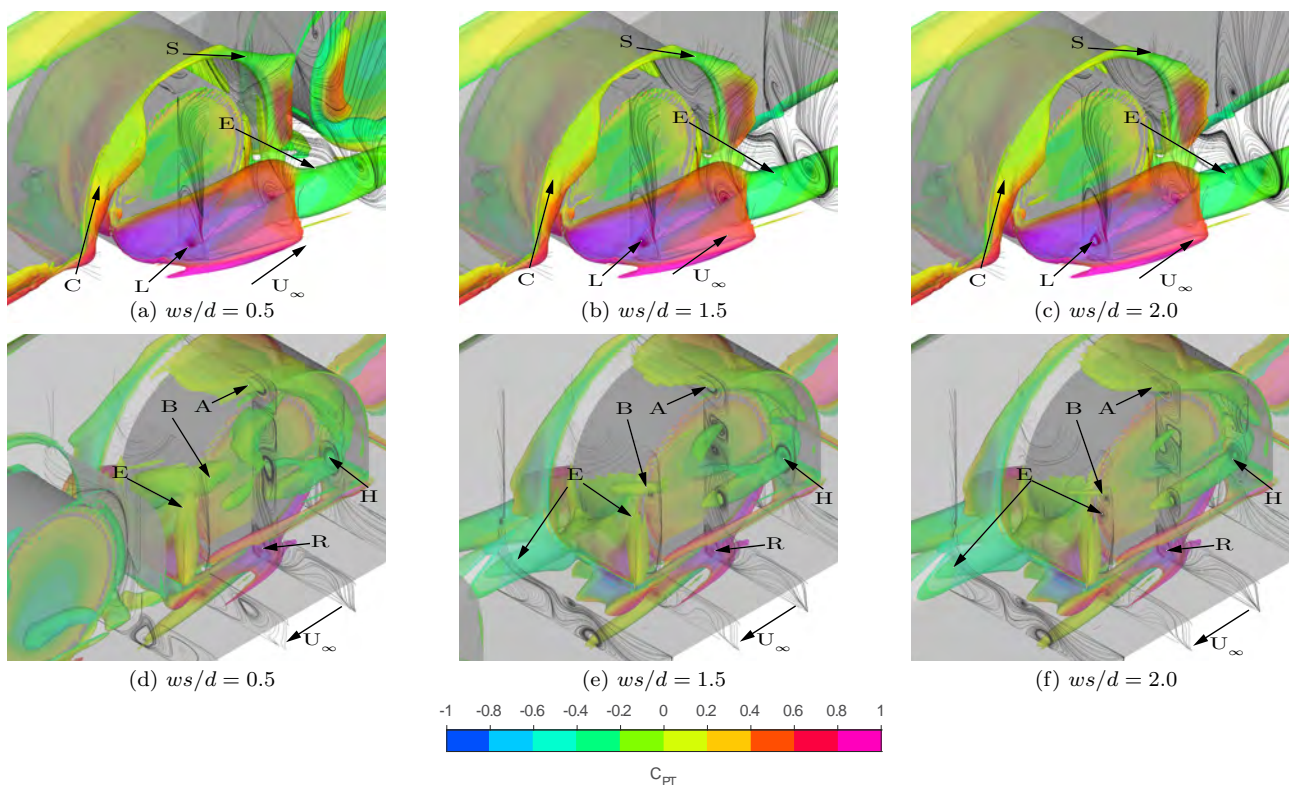
Figure 4.26: Vortex cores around the front wheel for varying wheel spacing with front overhang $le/d = 1.5$, plotted with $Q = 3.2 \times 10^5 \ s^{-2}$, $\alpha = 0.45$
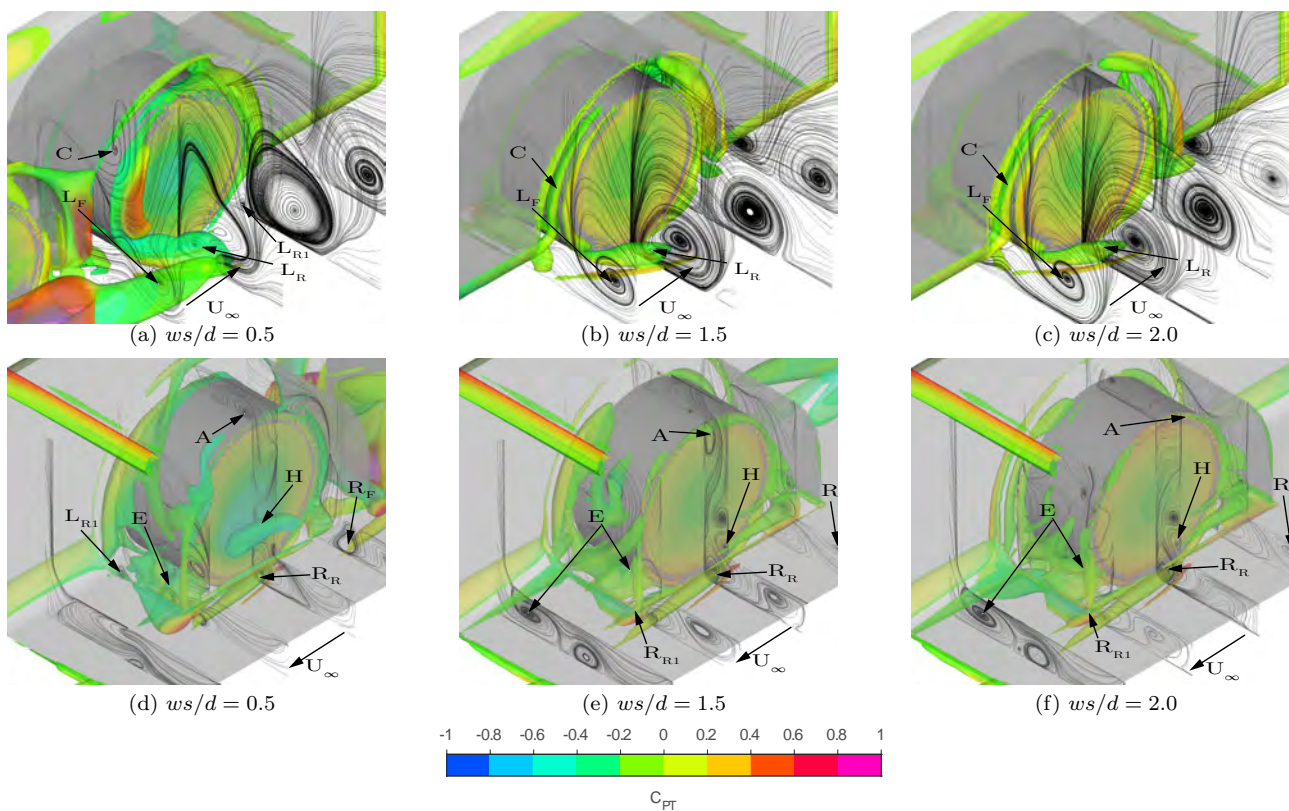


Figure 4.27: Vortex cores around the rear wheel for varying wheel spacing with front overhang $le/d = 1.5$, plotted with $Q = 3.2 \times 10^5 \ s^{-2}$, $\alpha = 0.45$

the inner wheelhouse has much greater variation than the flow structures outboard of the body. The C vortex is drawn inwards towards the end of the H vortex at the back of the inner wheelhouse to merge with the E vortex for $ws/d < 1.5$, reducing the strength of the S vortex of the rear wheelhouse. Vortices A and B do not appear in the rear wheelhouse for any of the tested cases and is a result of the disrupted H vortex which remains in the lower portions of the wheelhouse before merging with the vortex R and E.



Figure 4.28: Flow features within the rear wheelhouse for varying wheel spacing with front overhang $le/d = 1.5$; (a-c) $x_{rw}/d = -0.5$; (d-f) $x_{rw}/d = 0$; (g-i) $x_{rw}/d = 0.5$

The core of vortex L is significantly larger for $ws/d = 0.5$ (figure 4.28c) than the longer wheel

spaced cases, yet dissipates at a similar location to the other cases downstream whereas vortex R appears to be less affected by the upstream flow. Vortex A causes the primary outflow from the upper wheelhouse while vortex B appears to remain relatively suppressed. The weak rotations of vortex C are only noticed for $ws/d = 0.5$ before being dissipating into vortex A. Vortex H moves towards the inner wheelhouse for $ws/d = 1.5$ and merges with Vortex E towards the back of the wheelhouse. The position of Vortex E varies for each case, moving further inboard for $ws/d > 1.5$ (figures 4.28g, 4.28h, 4.28i).



(a) $ws/d = 0.5$       (b) $ws/d = 1.5$       (c) $ws/d = 3.0$

(d) $ws/d = 0.5$       (e) $ws/d = 1.5$       (f) $ws/d = 3.0$
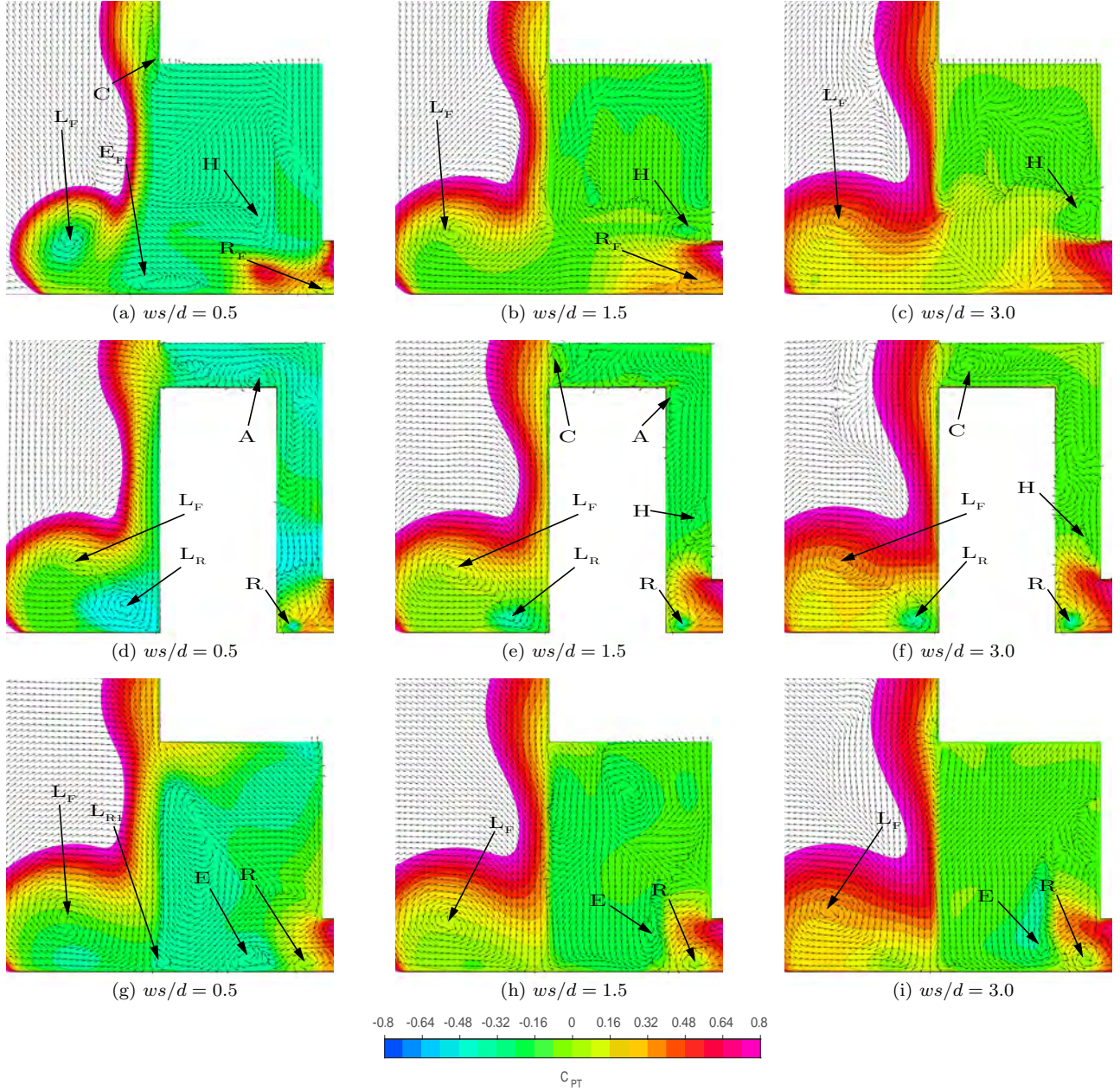
-0.8   -0.64   -0.48   -0.32   -0.16   0   0.16   0.32   0.48   0.64   0.8

$C_{PT}$
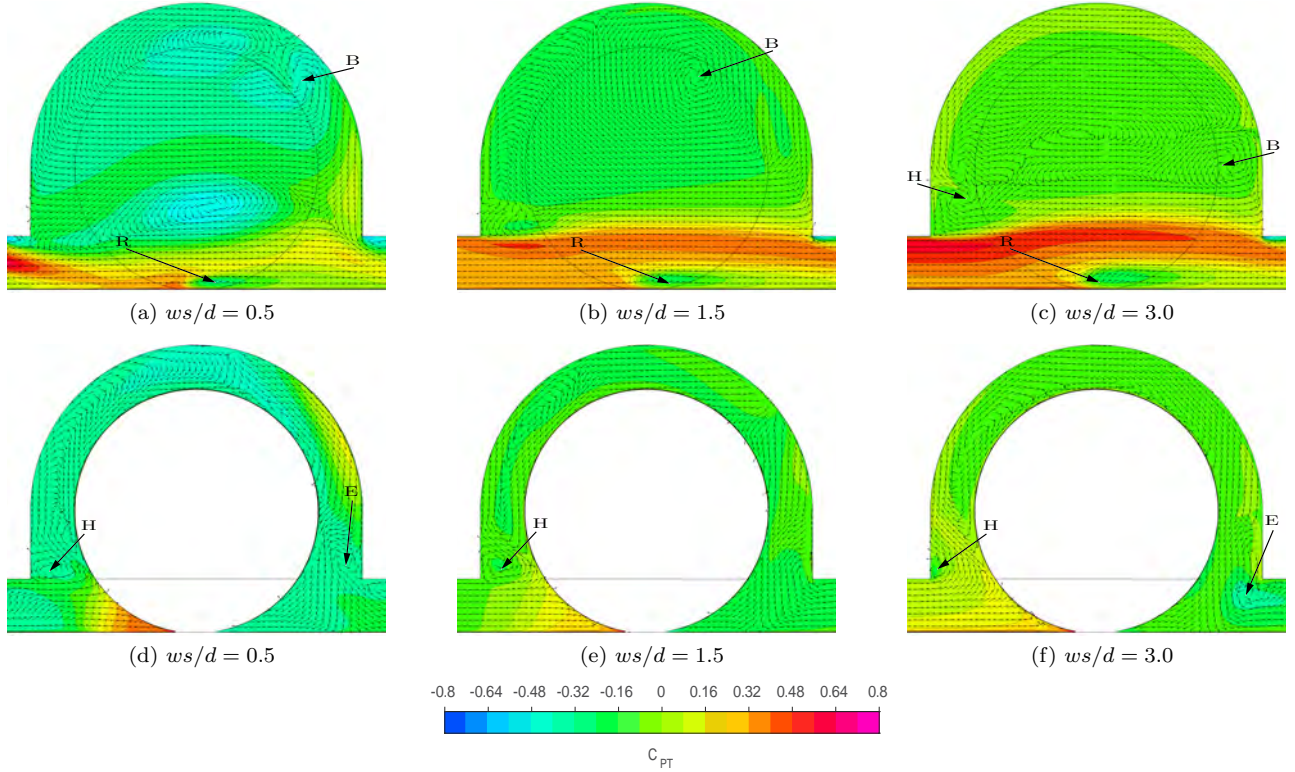
Figure 4.29: Flow through the rear wheelhouse for varying wheel spacing with front overhang $le/d = 1.5$; (a-c) $y/d = 0.68$; (d-f) $y/d = 1$

Vortex B experiences the most significant spatial displacement through the inner wheelhouse as it moves from the upper wheelhouse for $ws/d = 0.5$ towards the rear of the wheelhouse for $ws/d = 3$ (figures 4.29a-4.29c). Vortex H has a larger core, spanning from the front of the wheelhouse to the wheel surface and creating a larger recirculation above that impedes the formation of vortex A for $ws/d = 0.5$ (figure 4.29d). The vortex core reduces in size for $ws/d > 1.5$ and moves closer to the front of the wheelhouse and has less effect on the rotation above the wheel (figures 4.29e, 4.29f). This results in a general flow through the rear wheelhouse with less rotation and more downflow towards the underbody, similar to flow for the $ws/d = 1$ overhang cases.

Recirculation behind the rear wheel does not project as far in the spanwise direction as was the
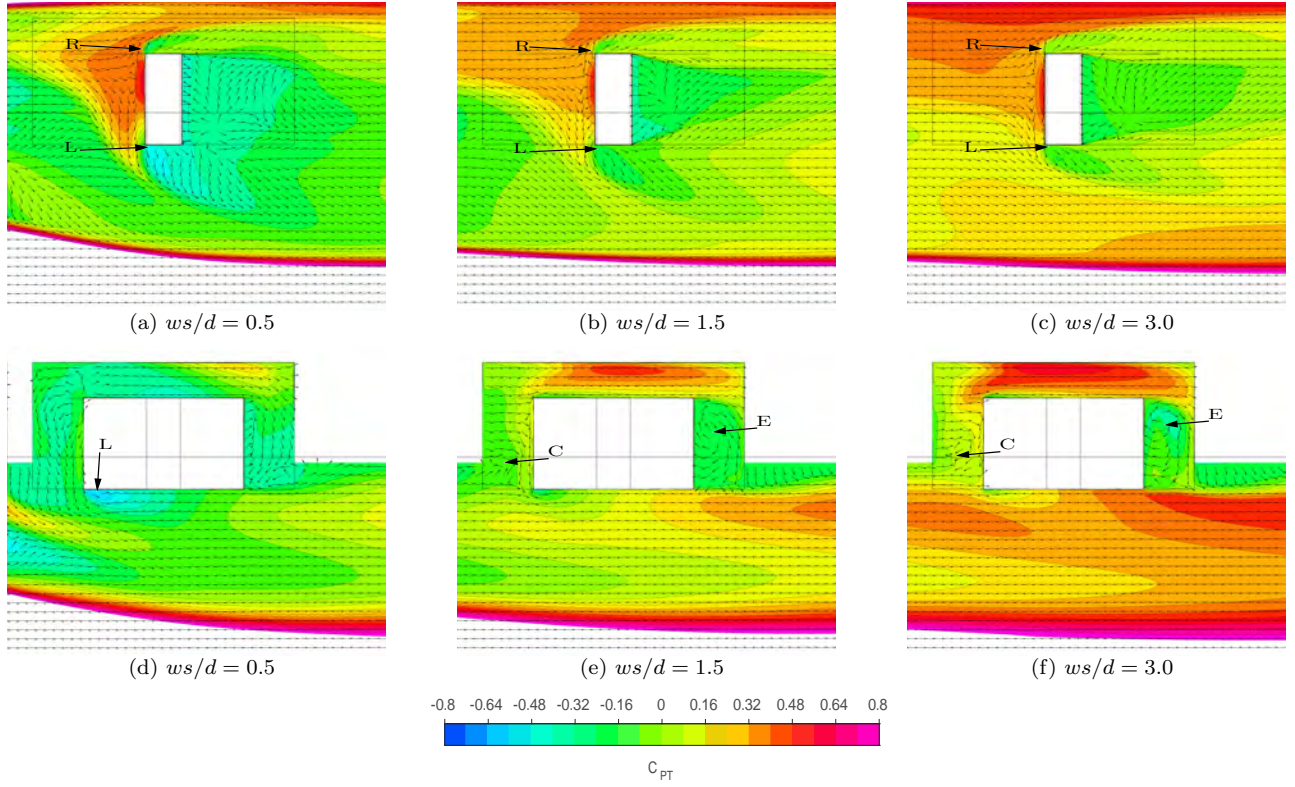
Figure 4.30: (a-c) Flow at the wheel-ground contact patch for varying wheel spacing with front overhang $le/d = 1.5$; (d-f) Wheelhouse outlflow inline with the underbody $z/d = 0.22$

case with front overhangs $ws/d < 1.5$ and tends to follow the freestream flow (figure 4.30). Outflow from the front of the wheelhouse is only noticed for $ws/d = 0.5$ and aids vortex L to form higher up the wheel shoulder (figure 4.30d). Other cases experience rotation from a small C vortex that keeps vortex L near the lower shoulder of the wheel. Flow exiting the wheelhouse exhibits similar rotation at the rear of the wheelhouse for $ws/d > 1.5$, with flow moving in the freestream direction as a result of the undisturbed L vortex generated by the front wheel. This leads to an overall lower drag for longer front overhang bodies and less adverse effects at the rear wheel and wheelhouse.

# Chapter 5

# Conclusion

The Fabijanic reference model was modified to incorporate an additional wheel placed towards the rear of the body, producing a new baseline geometry for this study. Space between the wheels was set at three wheel diameters as a baseline and then varied from 0.5 to 6 wheel diameters while the front and rear overhang were held constant. The addition of the rear wheel increased total drag with clear differences in key flow structures observed between the front and rear wheelhouse. The outboard jetting vortex from the wheel, vortex L, creates a large wake outboard of the rear wheel which influences the formation of the wheelhouse arch vortex C and rear wheel outboard jetting vortex as wheel spacing reduces, resulting in a drag reduction across the rear wheel. Primary outflow from the inner wheelhouse of the front wheel into the underbody significantly affects the vortex rolling up into the rear wheelhouse, vortex H, and the flowfield through the inner rear wheelhouse. The most significant change occurred when wheel spacing was reduced below 1.5 wheel diameters, where the change in rear wheelhouse flow structures generated a significant drag increase exceeding any drag force reduction at the rear wheel.

Variation in the front overhang length yielded significant changes to key flow structures around the front wheel. The shortest overhang produced the most drag of each variation investigated owing to the drastic change in the outboard jetting vortex. Flow structures between the wheel and wheelhouse were observed to be spatially displaced, being drawn towards the underbody instead of outboard of the wheelhouse and was observed to increase drag on the body. Longer front overhangs reduced outflow from the inner wheelhouse into the underbody, merging outboard with the jetting vortex, reducing drag substantially for these cases. Changes in the rear wheel flowfield were also less significant as front overhang was increased due to the formation of the outboard jetting vortex. In summary, a minimum drag configuration would minimise front wheelhouse outflow into the underbody preventing the outboard jetting vortex from being disrupted by yawed inflow into the wheelhouse.

Each front overhang variation was evaluated with varying wheel spacing and compared to the

initial study. Minimum drag force was observed at different wheel spacing for each overhang, demonstrating body drag force to be a function of the combined front overhang length and wheel spacing. These factors influence the size of the outboard jetting vortex, determining the formation of this vortex and according front wheel wake. For every case minimum drag was observed when the outboard jetting vortex was fully formed and minimally affected yawed flow in the front wheelhouse with the primary wheelhouse outflow projected away from the body.

## 5.1   Future Recommendations

The following recommendations are offered as logical progressions of this work:

- Validating the results of this study with a more comprehensive collection of experimental data to add further confidence to the ability of the computational model.

- Reducing the radius on the geometry between the leading face and underbody would allow for much shorter front overhangs to be studied. Front overhangs as small as $ws/d = 0.1$ need to be considered as these may occur across many heavy vehicles and some production cars where typical overhangs are between $ws/d = 0.25$ and $ws/d = 0.5$. A smaller wheelhouse diameter such as the $w_d = 1.14$ as validated in Chapter 3 is also recommended to be studied for its relevance to real-world automotive cases.

- Further investigation with the geometries tested in this study under various flow conditions such as cross-wind or cornering which are more representative of real-world flows. This will provide further insight into how yawed flows behave within the inner wheelhouse, particularly given the sensitivity of wheelhouse flow structures to yawed flow as observed throughout this study.

- Additional geometry modifications to influence the flow around the wheelhouse in an effort to reduce drag. Past authors have experimented with baffles and wheelhouse vents on generic and practical forms. Specific, intentional manipulation of the front wheel and wheelhouse vortex flow structures may lead to an overall reduction in drag force.

# References

[1]  T. C. Schuetz, *Aerodynamics of Road Vehicles, Fifth Edition*. 2015. DOI: `10.4271/r-430`.

[2]  P. Elofsson and M. Bannister, "Drag reduction mechanisms due to moving ground and wheel rotation in passenger cars," *SAE Tech. Pap.*, no. 724, 2002, ISSN: 26883627. DOI: `10.4271/2002-01-0531`.

[3]  T. Regert and T. Lajos, "Investigation of flow field past rotating wheels of cars," *Model. Fluid Flow, Budapest*, 2003. [Online]. Available: `http://www.ara.bme.hu/%7B~%7Dregert/publications/regert%7B%5C_%7Dlajos%7B%5C_%7Dcmff2003.pdf`.

[4]  S. Krajnović and J. Fernandes, "Numerical simulation of the flow around a simplified vehicle model with active flow control," *Int. J. Heat Fluid Flow*, vol. 32, no. 1, pp. 192–200, 2011, ISSN: 0142727X. DOI: `10.1016/j.ijheatfluidflow.2010.06.007`.

[5]  C. Hurst, *No Title*, 2019. [Online]. Available: `https://rennlist.com/how-tos/slideshows/rain-racing-with-legends-first-time-at-sonoma-557131%7B%5C#%7Dlesson-5-crowned-braking-zones` (visited on 08/11/2020).

[6]  J. Fabijanic, "An experimental investigation of wheel-well flows," *SAE Tech. Pap.*, pp. 161–172, 1996, ISSN: 26883627. DOI: `10.4271/960901`.

[7]  L. Axon, K. Garry, and J. Howell, "The Influence of Ground Condition on the Flow Around a Wheel Located Within a Wheelhouse Cavity," *SAE Tech. Pap. Ser.*, vol. 1, no. 724, 1999. DOI: `10.4271/1999-01-0806`.

[8]  A. F. Skea, P. R. Bullen, and J. Qiao, "CFD Simulations and Experimental Measurements of the Flow Over a Rotating Wheel in a Wheel Arch," *SAE Tech. Pap. Ser.*, vol. 1, no. 724, 2000. DOI: `10.4271/2000-01-0487`.

[9]  A. Wäschle, "The Influence of Rotating Wheels on Vehicle Aerodynamics - Numerical and Experimental Investigations," *SAE Tech. Pap. Ser.*, vol. 1, no. 724, pp. 776–790, 2007. DOI: `10.4271/2007-01-0107`.

[10]  A. Cogotti, "Aerodynamic characteristics of car wheels.," no. (Technol. Adv. in Vehicle Des. - Special Publication SP3-1983), 1983.

[11] T. Régert, A. Schwarczkopf, and T. Lajos, *The Effect of Wheels on the Aerodynamic Characteristics of an Ahmed Body*, Frankfurt, Germany, 2008.

[12] E. Thivolle-Cazat and P. Gilliéron, "Flow analysis around a rotating wheel," *13th Int. Symp. Appl. Laser Tech. to Fluid Mech.*, no. January 2006, pp. 26–29, 2006. [Online]. Available: `http://ltces.dem.ist.utl.pt/lxlaser/lxlaser2006/downloads/papers/15%7B%5C_%7D1.pdf`.

[13] T. Regert and T. Lajos, "Description of flow field in the wheelhouses of cars," *Int. J. Heat Fluid Flow*, vol. 28, no. 4, pp. 616–629, 2007, ISSN: 0142727X. DOI: `10.1016/j.ijheatfluidflow.2007.04.017`.

[14] J. Wiedemann, "The influence of ground simulation and wheel rotation on aerodynamic drag optimization-potential for reducing fuel consumption," in *SAE Tech. Pap.*, 1996. DOI: `10.4271/960672`.

[15] V. Viswanathan, "Aerodynamics of a rotating wheel in a wheelhouse," Master Thesis, Technische Universiteit Delft, 2017. [Online]. Available: `https://repository.tudelft.nl/islandora/object/uuid:2c964dfc-8b3d-44ba-9e3d-cd22704aa862?collection=education`.

[16] S. Krajnović, S. Sarmast, and B. Basara, "Numerical Investigation of the Flow Around a Simplified Wheel in a Wheelhouse," *J. Fluids Eng.*, vol. 133, no. 11, p. 111 001, 2011, ISSN: 00982202. DOI: `10.1115/1.4004992`.

[17] S. Krajnović and L. Davidson, "Large eddy simulation of the flow around an ahmed body," in *Proc. ASME Heat Transf. Eng. Summer Conf. 2004, HT/FED 2004*, 2004. DOI: `10.1115/ht-fed2004-56325`.

[18] A. Schwarczkopf, T. Regert, and T. Lajos, "Investigation of Simple Possibilities for Reduction of Drag due to the Wheels of Road Vehicles," *4th Eur. Automot. Simul. Conf. Munich,*, no. July, 2009.

[19] I. Dimitriou and S. Klussmann, "Aerodynamic Forces of Exposed and Enclosed Rotating Wheels as an Example of the Synergy in the Development of Racing and Passenger Cars," *SAE Tech. Pap. Ser.*, vol. 1, no. 724, 2010. DOI: `10.4271/2006-01-0805`.

[20] A. Gulyás, Á. Bodor, T. Regert, and I. M. Jánosi, "PIV measurement of the flow past a generic car body with wheels at LES applicable Reynolds number," *Int. J. Heat Fluid Flow*,

vol. 43, pp. 220–232, 2013, ISSN: 0142727X. DOI: `10.1016/j.ijheatfluidflow.2013.05.012`. [Online]. Available: `http://dx.doi.org/10.1016/j.ijheatfluidflow.2013.05.012`.

[21] S. Bonitz, L. Larsson, and S. Sebben, "Unsteady pressure analysis of the near wall flow downstream of the front wheel of a passenger car under yaw conditions," *Int. J. Heat Fluid Flow*, vol. 73, no. July, pp. 188–198, 2018, ISSN: 0142727X. DOI: `10.1016/j.ijheatfluidflow.2018.07.007`. [Online]. Available: `https://doi.org/10.1016/j.ijheatfluidflow.2018.07.007`.

[22] S. F. Hoerner, *Fluid-dynamic drag : practical information on aerodynamic drag and hydrodynamic resistance*, English. Midland Park, N.J.: Dr.-Ing. S.F. Hoerner, 1958.

[23] M. M. Alam, M. Moriya, K. Takai, and H. Sakamoto, "Fluctuating fluid forces acting on two circular cylinders in a tandem arrangement at a subcritical Reynolds number," *J. Wind Eng. Ind. Aerodyn.*, vol. 91, no. 1-2, pp. 139–154, 2003, ISSN: 01676105. DOI: `10.1016/S0167-6105(02)00341-0`.

[24] P. W. Bearman and A. J. Wadcock, "The interaction between a pair of circular cylinders normal to a stream," *J. Fluid Mech.*, vol. 61, no. 3, pp. 499–511, 1973, ISSN: 14697645. DOI: `10.1017/S0022112073000832`.

[25] D. Sumner, "Two circular cylinders in cross-flow: A review," *J. Fluids Struct.*, vol. 26, no. 6, pp. 849–899, 2010, ISSN: 08899746. DOI: `10.1016/j.jfluidstructs.2010.07.001`. [Online]. Available: `http://dx.doi.org/10.1016/j.jfluidstructs.2010.07.001`.

[26] T. Igarashi, "CHARACTERISTICS OF THE FLOW AROUND TWO CIRCULAR CYLINDERS ARRANGED IN TANDEM - 1.," *Bull. JSME*, vol. 24, no. 188, 1981, ISSN: 00213764. DOI: `10.1299/jsme1958.24.323`.

[27] S. Spagnolo, X. Zhang, Z. Hu, O. Stalnov, and D. Angland, "Unsteady aerodynamics of single and tandem wheels," *J. Fluids Struct.*, vol. 69, no. October 2016, pp. 121–136, 2017, ISSN: 10958622. DOI: `10.1016/j.jfluidstructs.2016.11.022`. [Online]. Available: `http://dx.doi.org/10.1016/j.jfluidstructs.2016.11.022`.

[28] S. Spagnolo, X. Zhang, Z. Hu, and D. Angland, "Numerical simulations of single and tandem wheels for aerodynamic loads prediction," *22nd AIAA Comput. Fluid Dyn. Conf.*, pp. 1–15, 2015. DOI: `10.2514/6.2015-3066`.

[29] M. R. Rasani, A. Shamsudeen, Z. Harun, and W. M. F. Wan Mahmood, "A computational aerodynamic study of tandem rotating wheels in contact with the ground," *Int. J. Eng.*

*Technol.*, vol. 7, no. 3, pp. 133–136, 2018, ISSN: 2227524X. DOI: `10.14419/ijet.v7i3.17.16637`.

[30] J. E. Fackrell, "The Aerodynamics of an Isolated Wheel Rotating in Contact with the Ground," PhD Thesis, University of London, 1974.

[31] S. Diasinos, T. J. Barber, and G. Doig, "The effects of simplifications on isolated wheel aerodynamics," *J. Wind Eng. Ind. Aerodyn.*, vol. 146, no. 1975, pp. 90–101, 2015, ISSN: 01676105. DOI: `10.1016/j.jweia.2015.08.004`.

[32] W. R. Stapleford, G. W. Carr, and M. I. R. Association., *Aerodynamic characteristics of exposed rotating wheels*, English. Lindley [England]: Motor Industry Research Association, 1969.

[33] L. Axon, K. Garry, and J. Howell, "An Evaluation of CFD for Modelling the Flow Around Stationary and Rotating Isolated Wheels," *SAE Tech. Pap. Ser.*, vol. 1, no. 724, 1998. DOI: `10.4271/980032`.

[34] Krishna Ramani sri, "Experimental Investigation of Wheelhouse flow using PIV," Master Thesis, Technische Universiteit Delft, 2018. [Online]. Available: `https://repository.tudelft.nl/islandora/object/uuid:f37dc203-6fce-488d-926f-c2b30be5caf9?collection=education`.

[35] J. Wiedemann and J. Potthoff, "The new 5-belt road simulation system of the IVK wind tunnels - Design and first results," *SAE Tech. Pap.*, vol. 2003, no. 724, 2003, ISSN: 26883627. DOI: `10.4271/2003-01-0429`.

[36] G. M. Le Good and K. P. Garry, "On the use of reference models in automotive aerodynamics," *SAE Tech. Pap.*, vol. 2004, no. 724, 2004, ISSN: 26883627. DOI: `10.4271/2004-01-1308`.

[37] A. I. Heft, T. Indinger, and N. A. Adams, "Introduction of a New Realistic Generic Car Model for Aerodynamic Investigations," 2012. DOI: `10.4271/2012-01-0168`.

[38] S. Krajnović and L. Davidson, "Numerical study of the flow around a bus-shaped body," *J. Fluids Eng. Trans. ASME*, vol. 125, no. 3, pp. 500–509, 2003, ISSN: 00982202. DOI: `10.1115/1.1567305`.

[39] T. H. Shih, W. W. Liou, A. Shabbir, Z. Yang, and J. Zhu, "A new k- eddy viscosity model for high reynolds number turbulent flows," *Comput. Fluids*, vol. 24, no. 3, pp. 227–238, 1995, ISSN: 00457930. DOI: `10.1016/0045-7930(94)00032-T`.

[40] J. McManus and X. Zhang, "A computational study of the flow around an isolated wheel in contact with the ground," *J. Fluids Eng. Trans. ASME*, vol. 128, no. 3, pp. 520–530, 2006, ISSN: 00982202. DOI: 10.1115/1.2175158.

[41] C. Zhang, C. P. Bounds, L. Foster, and M. Uddin, "Turbulence modeling effects on the CFD predictions of flow over a detailed full-scale sedan vehicle," *Fluids*, vol. 4, no. 3, pp. 1–28, 2019, ISSN: 23115521. DOI: 10.3390/fluids4030148.

[42] K. Forster, "The Interactions of Streamwise , Co-rotating and Counter-rotating Vortices," Ph.D. dissertation, University of New South Wales, 2018.

[43] N. Lindener, H. Miehling, A. Cogotti, F. Cogotti, and M. Maffei, "Aeroacoustic measurements in turbulent flow on the road and in the wind tunnel," *SAE Tech. Pap.*, vol. 2007, no. 724, pp. 776–790, 2007, ISSN: 26883627. DOI: 10.4271/2007-01-1551.

[44] H. K. Versteeg and W. Malalasekera, *An Introduction to Computational Fluid Dynamics 2nd Edition*, 5. 2007, vol. 7. DOI: 10.2514/1.22547.

[45] ANSYS Inc., *ANSYS Fluent Theory Guide*. 2018.

[46] P. Roache, "A Method for Uniform Reporting of Grid Refinement Studies," *J. Fluids Eng.*, vol. 116, pp. 405–413, 1994, ISSN: 1098-6596. DOI: 10.1017/CBO9781107415324.004. arXiv: arXiv:1011.1669v3.